

THE SCALING RELATIONS AND THE FUNDAMENTAL PLANE FOR RADIO HALOS AND RELICS OF GALAXY CLUSTERS

Z. S. YUAN^{1,2}, J. L. HAN¹, Z. L. WEN¹

¹National Astronomical Observatories, Chinese Academy of Sciences, 20A Datun Road, Chaoyang District, Beijing 100012, China; hjl@nao.cas.cn

²School of Physics, University of Chinese Academy of Sciences, Beijing 100049, China

Draft version July 30, 2018

ABSTRACT

Diffuse radio emission in galaxy clusters is known to be related to cluster mass and cluster dynamical state. We collect the observed fluxes of radio halos, relics, and mini-halos for a sample of galaxy clusters from the literature, and calculate their radio powers. We then obtain the values of cluster mass or mass proxies from previous observations, and also obtain the various dynamical parameters of these galaxy clusters from optical and X-ray data. The radio powers of relics, halos, and mini-halos are correlated with the cluster masses or mass proxies, as found by previous authors, with the correlations concerning giant radio halos being, in general, the strongest ones. We found that the inclusion of dynamical parameters as the third dimension can significantly reduce the data scatter for the scaling relations, especially for radio halos. We therefore conclude that the substructures in X-ray images of galaxy clusters and the irregular distributions of optical brightness of member galaxies can be used to quantitatively characterize the shock waves and turbulence in the intracluster medium responsible for re-accelerating particles to generate the observed diffuse radio emission. The power of radio halos and relics is correlated with cluster mass proxies and dynamical parameters in the form of a fundamental plane.

Subject headings: galaxies: clusters: general — galaxies: clusters: intracluster medium

1. INTRODUCTION

Clusters of galaxies are the largest gravitationally bound systems in the universe, formed at knots of cosmic webs in the universe. Diffuse radio emission has been detected from about 100 galaxy clusters. Based on their morphology, location, and size, the diffuse radio sources are classified as radio halos, radio relics, or mini-halos (see Feretti et al. 2012 for an observational review). Radio halos are located at the cluster center and unpolarized (< 10%), and have a regular morphology with a typical scale of about 1 Mpc. Radio relics usually also have a similar size, but are located in peripheral regions of galaxy clusters and often polarized (~20-30%). Mini-halos are detected in the central regions of clusters with no obvious polarization, but have a smaller size (\lesssim 500 kpc). Radio halos and relics are clearly related to cluster mergers (e.g., Cassano et al. 2010; Cuciti et al. 2015), while mini-halos are detected in cool-core galaxy clusters (e.g., Cassano et al. 2010; van Weeren et al. 2010; Kale et al. 2015). Both mini-halos and giant radio halos are detected from clusters with high X-ray luminosity (Kale et al. 2015). Observations of diffuse radio emission of clusters open a new window to study the intracluster medium, especially the particle accelerations and magnetic field amplification of galaxy clusters with different dynamical states (see Brunetti & Jones 2014 for a review).

Strong correlations have been found between the radio power at 1.4 GHz, $P_{1.4 \text{ GHz}}$, of radio halos and other physical cluster parameters, namely the cluster X-ray luminosity, L_X , and hot gas temperature, T_X (e.g., Liang et al. 2000; Brunetti et al. 2007, 2009; Cassano et al. 2013). Mini-halos also follow a similar relation between radio power and the cluster X-ray luminosity (Cassano et al. 2008; Kale et al. 2013, 2015). Correlations between $P_{1.4 \text{ GHz}}$ of radio relics and the cluster X-ray luminosity have also been found (e.g., Feretti et al. 2012; de Gasperin et al. 2014). However, radio

halos are detected only from only 20% to 30% of massive clusters with high X-ray luminosity (e.g., Kale et al. 2013, 2015). Brunetti et al. (2007, 2009) first discovered this radio bimodality that galaxy clusters with radio halos follow the correlation between the radio power and cluster X-ray luminosity, while clusters with non-detection of radio halos should have a radio power much below the correlation line. These two populations of clusters are found to correspond to different dynamical states, i.e., clusters with radio halos showing merging features and those without radio halos being more relaxed in general (e.g., Cassano et al. 2010).

Because the X-ray luminosity and gas temperature of galaxy clusters are tightly related to cluster mass, the relations of $P_{1.4 \text{ GHz}}-L_X$ and $P_{1.4 \text{ GHz}}-T_X$ may indicate that emission of halos and mini-halos is fundamentally related to cluster mass. The Sunyaev-Zel'dovich (SZ) parameter, indicated as Y_{SZ} , is a better mass proxy than the X-ray luminosity, since it is less affected by the cluster dynamics (e.g., Motl et al. 2005; Wik et al. 2008; Arnaud et al. 2010; Planck Collaboration et al. 2014a). Basu (2012) found a tight correlation between the radio power $P_{1.4 \text{ GHz}}$ from the literature and Y_{SZ} from the early Planck SZ catalog. By using updated SZ data from the Planck mission (Planck Collaboration et al. 2014b) and radio measurements from the GMRT cluster survey, Cassano et al. (2013) confirmed the scaling relation between the radio power and the cluster SZ parameter and also the radio bimodality in the radio-SZ diagram for massive clusters.

There are indications that radio halos, mini-halos, and relics in galaxy clusters are related to not only cluster masses but also dynamical states of clusters (e.g., Cuciti et al. 2015). Recently, Wen & Han (2013) found that the offset of radio power from the $P_{1.4 \text{ GHz}}-L_X$ relation is closely related to the dynamical parameter Γ defined from the optical galaxy luminosity distributions (see Sect. 2.3). To extend previous studies, in this paper we search for an empirical fundamental plane

among three sets of quantities: the synchrotron radio power of halos, relics, and mini-halos, the cluster mass represented by X-ray luminosity or estimated from gas mass and the SZ effect, and the cluster dynamical state obtained quantitatively from X-ray or optical data. In Sect.2, we calculate the observed radio power of halos, relics, and mini-halos at three frequencies, 1.4 GHz, 610 MHz, and 325 MHz, and collect the mass proxies of galaxy clusters, L_X and L_{500} , and also the SZ-estimated mass $M_{500, \text{SZ}}$ and the mass M_{500} estimated from gas mass, and obtain the dynamical parameters, Γ , c , ω , and P_3/P_0 , for a large sample of galaxy clusters with detected radio halos, relics, and mini-halos. In Section 3, we compare the data scatter around different scaling relations and then search for the fundamental plane in the three-dimensional space of these parameters. Conclusions and discussions are presented in Section 4.

Throughout this paper, we assume a Λ CDM cosmology, taking $H_0 = 100 h \text{ km s}^{-1} \text{ Mpc}^{-1}$, with $h = 0.7$, $\Omega_m = 0.3$, and $\Omega_\Lambda = 0.7$. Derived parameters in the literature have been scaled to this cosmology.

2. THREE SETS OF DATA FOR GALAXY CLUSTERS

In this section, we collect and rescale the values of radio flux and power in Table 1 and cluster mass and the cluster dynamical state for 75 galaxy clusters in Table 2 for further analyses.

2.1. Radio Power of Radio Halos, Relics, and Mini-halos

A large number of radio halos, relics, and mini-halos have been discovered and measured in recent decades through observations with VLA (e.g., Giovannini & Feretti 2000; van Weeren et al. 2011b), GMRT (e.g., Venturi et al. 2007; Kale et al. 2015), WSRT (e.g., van Weeren et al. 2010; Trasatti et al. 2015) and also ATCA (e.g., Shimwell et al. 2014, 2015). We have checked the radio images of radio halos, relics, and mini-halos in the literature and collected in Table 1 the radio flux S_ν at frequencies within a few per cent around 1.4 GHz, 610 MHz, and 325 MHz; we have interpolated the flux at an intermediate frequency if measurements are available at higher and lower frequencies. To establish the reliable scaling relations, we include only the very firm detection of diffuse radio emission in galaxy clusters, and omit the questionable detections or flux estimates due to problematic point-source subtraction. We then calculate the radio power via

$$P_\nu = 4\pi D_L^2 \times S_\nu \times (1+z)^{1-a}, \quad (1)$$

where $D_L = (1+z)c/H_0 \int_0^z \frac{dz'}{\sqrt{\Omega_m(1+z')^3 + \Omega_\Lambda}}$ is the luminosity distance of a cluster at a redshift of z , S_ν is the radio flux at frequency ν , $(1+z)^{1-a}$ is the k -correction term as done by Cassano et al. (2013), and a is the spectral index of diffuse radio sources, which is assumed to be 1.3 in general.

2.2. Mass Proxies and Mass Estimates for Galaxy Clusters

The total X-ray luminosities, L_X , of galaxy clusters and the X-ray luminosities, L_{500} , within R_{500} are most often used as mass proxies for galaxy clusters. Here, R_{500} is the radius of a galaxy cluster within which the matter density of a cluster is 500 times of the critical density of the universe. In Table 2, we collect these two X-ray measurements for galaxy clusters with diffuse radio emission. The total X-ray luminosities of galaxy clusters, L_X , were derived from observations in the 0.1-2.4 keV band and taken from catalogs based

on the *ROSAT* All-Sky Survey data (e.g., Ebeling et al. 1996, 1998, 2000; Böhringer et al. 2000, 2004). The collected X-ray luminosities within R_{500} of the clusters, L_{500} , are the values updated by using the new measurements from deep *Chandra* or *XMM-Newton* images from Mantz et al. (2010), Cassano et al. (2013), and Zhao et al. (2015).

Masses of galaxy clusters can be estimated from the SZ measurements of the integrated Compton parameter $Y_{\text{SZ}, 500}$ within R_{500} via

$$Y_{\text{SZ}, 500} = d_A^2(z)Y = Q(\Omega_m(1+z)^3 + \Omega_\Lambda)^{1/3} M_{\text{SZ}, 500}^\kappa, \quad (2)$$

where $d_A(z)$ is the angular diameter distance to clusters, Y is the integrated Compton parameter, and $M_{\text{SZ}, 500}$ is the mass within R_{500} estimated from the SZ effect, $\log Q = -0.19$, and $\kappa = 1.79$ (Planck Collaboration et al. 2014a). Note that the $Y_{\text{SZ}, 500}$ and $M_{\text{SZ}, 500}$ are scaled by a power index $\kappa = 1.79$. The largest SZ-selected catalog to date is the all-sky Planck catalog of galaxy clusters, which contains 1653 clusters with redshifts up to $z \sim 1$ (Planck Collaboration et al. 2015). In this paper we take the mass estimates $M_{\text{SZ}, 500}$ directly from Planck Collaboration et al. (2015) for galaxy clusters.

In the literature, cluster mass M_{500} has often been derived by using three X-ray proxies: average temperature T_X , gas mass M_{gas} , and $Y_X = T_X \times M_{\text{gas}}$ (e.g., Vikhlinin et al. 2009; Zhao et al. 2015). Another mass estimate used in this paper as one of four independent mass proxies in Table 2 is the cluster mass derived from the observed gas mass. We take M_{500} from Vikhlinin et al. (2009) and Mantz et al. (2010), obtained from the high-quality X-ray images and spectra of *Chandra* and *XMM* data. The systematic offset between the mass values in these two catalogs has been corrected according to Wen & Han (2015).

2.3. Dynamical Parameters of Galaxy Clusters

Wen & Han (2013) developed a method to quantify dynamical states of galaxy clusters from optical photometric data. They smoothed the brightness distribution of member galaxies using a Gaussian kernel with a weight of optical luminosity, and then defined a dynamical parameter Γ from the asymmetry, the normalized model-fitting residual, and the ridge-flatness of the smoothed optical image. They obtained Γ values for 98 clusters with qualitatively known “relaxed” or “unrelaxed” dynamical states, and then also for 2092 rich clusters of $M_{200} \geq 3.15 \times 10^{14} M_\odot$ in the cluster catalog of Wen et al. (2012). We quoted Γ in Table 2 from Wen & Han (2013) for 58 galaxy clusters with detected radio halos, relics, and mini-halos, and also calculated Γ values for the remaining 23 galaxy clusters that are not included in Wen & Han (2013).

Dynamical parameters have also been derived quantitatively from X-ray images of clusters by previous authors, including the concentration parameter c (e.g., Santos et al. 2008), the centroid shift ω (e.g., Poole et al. 2006), and the power ratio P_3/P_0 (e.g., Buote & Tsai 1995; Böhringer et al. 2010; Weißmann et al. 2013). The concentration parameter c is defined as the ratio of the peak to the ambient surface brightness as

$$c = \frac{S(R < 100\text{kpc})}{S(R < 500\text{kpc})}. \quad (3)$$

The centroid shift ω is defined as the standard deviation of the projected separation between the X-ray peak and the centroid in units of $R_{\text{ap}} = 500\text{kpc}$, which is computed in a series

TABLE 1
RADIO FLUX AND POWER FOR RADIO HALOS, RELICS, AND MINI-HALOS FROM 75 GALAXY CLUSTERS

Name (1)	z (2)	Type (3)	Size (4)	$S_{1.4}$ GHz (5)	S_{610} MHz (6)	S_{325} MHz (7)	References (8)	$\log P_{1.4}$ GHz (9)	$\log P_{610}$ MHz (10)	$\log P_{325}$ MHz (11)
A209	0.2060	halo	7'	15.0±0.7	24.0±3.6	...	1/ 2/ -	0.24±0.02	0.45±0.07	...
A399	0.0718	halo	7'	16±2	3/ -/ -	-0.70±0.06
A520	0.1990	halo	5.5'	16.7±0.6	42±15	85±5	4/ 0/ 4	0.26±0.02	0.66±0.19	0.96±0.03
A521	0.2533	halo(+relic)	5'	6.4±0.6	15±4	90±7	5/ 6/ 6	0.07±0.04	0.44±0.13	1.22±0.04
A545	0.1540	halo	5.6'	23±1	7/ -/ -	0.15±0.02
A665	0.1819	halo	10'	43.1±2.2	8/ -/ -	0.58±0.02
A697	0.2820	halo	2.5'	5.2±0.5	13.0±2.0	47.3±2.7	9/ 2/ 10	0.08±0.04	0.48±0.07	1.04±0.03
A746	0.2320	halo(+relic)	4'	18±4	9/ -/ -	0.43±0.11
A754	0.0542	halo(+relic)	16'	83±5 ^a	284±17	722±41	11/ 0/ 11	-0.24±0.03	0.29±0.03	0.70±0.03
A773	0.2170	halo	6'	12.7±1.3	12/ -/ -	0.22±0.05
A1300	0.3072	halo(+relic)	4.8'	130±10	-/-/ 1	1.56±0.03
A1351	0.3224	halo	3'	32.4±4.0	13/ -/ -	1.01±0.06
A1689	0.1832	halo	4'	9.6±2.8 ^b	14/ -/ -	-0.06±0.15
A1758N	0.2790	halo	6'	23±5	...	155±12	1/ -/ 1	0.72±0.11	...	1.55±0.03
A1914	0.1712	halo	7.5'	64±3	7/ -/ -	0.70±0.02
A1995	0.3186	halo	3'	4.1±0.7	15/ -/ -	0.10±0.08
A2069	0.1160	halo	5'	25±9	-/-/ 16	-0.07±0.19
A2163	0.2030	halo	11'	155±2	411±5	861±10	17/ 0/ 18	1.24±0.01	1.67±0.01	1.99±0.01
A2218	0.1756	halo	2'	4.7±0.1	8/ -/ -	-0.41±0.01
A2219	0.2256	halo	8'	81±4	7/ -/ -	1.06±0.02
A2255	0.0806	halo(+relic)	10'	56±3	194±10	496±7	19/ 0/ 20	-0.06±0.02	0.48±0.02	0.89±0.01
A2256	0.0581	halo(+relic)	12'	103.4±1.1	322±3	760±70	21/ 0/ 22	-0.08±0.01	0.41±0.01	0.78±0.04
A2319	0.0557	halo	16'	240±10	23/ -/ -	0.24±0.02
A2744	0.3080	halo(+relic)	7'	57±3	153±8	323±26	1/ 0/ 1	1.21±0.02	1.64±0.02	1.96±0.04
A3562	0.0490	halo	5'	20±2	90±9	195±39	24/25/25	-0.95±0.05	-0.30±0.05	0.04±0.10
Bullet	0.2960	halo	8'	56.4±2.3	26/ -/ -	1.16±0.02
CL0016+16	0.5456	halo	2.5'	5.5±0.8 ^c	8/ -/ -	0.76±0.07
CL0217+70	0.0655	halo	10'	58.6±0.9	156±2	326±30	27/ 0/ 27	-0.22±0.05	0.20±0.01	0.52±0.04
CL1821+643	0.299	halo	4'	14.3±0.7	33±2	62±4	0/ 0/ 28	0.58±0.02	0.94±0.03	1.22±0.03
Coma	0.0231	halo(+relic)	30'	530±50	1200±300	3180±30	29/30/31	-0.19±0.04	0.16±0.12	0.58±0.01
MACS J0553-3342	0.431	halo	4'	62±5	-/-/ 32	1.57±0.04
MACS J0717+3745	0.5458	halo	4'	118±5	162±0.23	337.5±0.5	33/34/ -	2.09±0.02	2.23±0.01	2.55±0.01
MACS J1752+4440	0.366	halo(+relic)	3.3'	164±13	-/-/ 32	1.84±0.04
PLCK G171.9-40.7	0.270	halo	5.5'	18±2	35/ -/ -	0.58±0.05
PLCK G287.0+32.9	0.39	halo(+relic)	4'	3.6±0.5 ^c	26±4 ^c	63±10 ^c	0/36/36	0.24±0.06	1.10±0.07	1.48±0.08
RXC J0107+5408	0.1066	halo	9.5'	55±5	9/ -/ -	0.19±0.04
RXC J1314-2515	0.2439	halo(+relic)	7'	...	10.3±0.3	40±3	-/ 2/ 1	...	0.24±0.01	0.83±0.03
RXC J1514-1523	0.2226	halo	7'	10±2	37±8	102±9	37/ 0/ 37	0.14±0.10	0.71±0.11	1.15±0.04
RXC J2003.5-2323	0.3173	halo	5'	35±2	96.9±5.0	235±12	38/ 2/ 0	1.03±0.03	1.47±0.02	1.85±0.02
Toothbrush	0.225	halo	9'	35.9±2.6	51.5±7.4	121.6±13.5	39/39/39	0.70±0.03	0.86±0.07	1.23±0.05
Z5247	0.229	halo(+relic)	4'	2±0.3	7.9±1	...	40/40/ -	-0.53±0.07	0.06±0.06	...
A115	0.1971	relic	12.5'	14.7±2.2 ^c	12/ -/ -	0.19±0.07
A521	0.2533	relic(+halo)	4.2'	15.0±0.8	41.9±2.1	114±6	41/ 2/ 1	0.44±0.02	0.89±0.02	1.32±0.02
A746	0.2320	relic(+halo)	5'	24.5±2.0	9/ -/ -	0.57±0.04
A754	0.0542	relic(+halo)	13'	6.0±0.3	31±2	106±5	11/ 0/ 11	-1.38±0.02	-0.67±0.03	-0.14±0.02
A1240-N	0.1590	relic	4'	6.0±0.2	12.2±0.4	21.0±0.8	42/ 0/ 42	-0.40±0.01	-0.09±0.01	0.14±0.02
A1240-S	0.1590	relic	7.5'	10.1±0.4	18.2±0.7	28.5±1.1	42/ 0/ 42	-0.17±0.02	0.08±0.02	0.28±0.02
A1300	0.3072	relic(+halo)	2.5'	75±6	-/-/ 1	1.32±0.04
A1612	0.179	relic	4.3'	62.8±2.6	9/ -/ -	0.73±0.02
A2061	0.0784	relic	7.5'	27.6±1.0	9/ -/ -	-0.39±0.02
A2255	0.0806	relic(+halo)	8'	23±1	58±3	117±2	19/ 0/ 20	-0.44±0.02	-0.04±0.02	0.26±0.01
A2256-G	0.0581	relic(+halo)	5'	231.6±15.1	447±30	735.7±45.8	43/ 0/ 43	0.27±0.03	0.55±0.03	0.77±0.03
A2256-H	0.0581	relic(+halo)	5'	245.8±19.1	475±37	781.3±64.3	43/ 0/ 43	0.29±0.04	0.58±0.04	0.79±0.04
A2345-E	0.1765	relic	8.5'	29.0±0.4	84±1	188±3	42/ 0/ 42	0.38±0.01	0.84±0.01	1.19±0.01
A2345-W	0.1765	relic	6.5'	30.0±0.5	109±2	291±4	42/ 0/ 42	0.40±0.01	0.96±0.01	1.38±0.01
A2744	0.3080	relic(+halo)	6'	20±1	54±8	122±10	1/ 0/ 1	0.75±0.02	1.18±0.07	1.54±0.04
A3365-E	0.0926	relic	5.5'	42.6±2.6	9/ -/ -	-0.05±0.03
A3365-W	0.0926	relic	2.3'	5.3±0.5	9/ -/ -	-0.95±0.01
A3376-E	0.0456	relic	16'	122±10	559±46	1770±90	44/ 0/ 44	-0.23±0.04	0.43±0.04	0.93±0.02
A3376-W	0.0456	relic	15'	113±10	467±41	1367±70	44/ 0/ 44	-0.26±0.04	0.35±0.04	0.82±0.02
A3667-SE	0.0556	relic	20'	350±20	45/ -/ -	0.41±0.03
A3667-NW	0.0556	relic	30'	2470±170	45/ -/ -	1.25±0.03

TABLE 1
continued

Name (1)	z (2)	Type (3)	Size (4)	$S_{1.4\text{ GHz}}$ (5)	$S_{610\text{ MHz}}$ (6)	$S_{325\text{ MHz}}$ (7)	References (8)	$\log P_{1.4\text{ GHz}}$ (9)	$\log P_{610\text{ MHz}}$ (10)	$\log P_{325\text{ MHz}}$ (11)
CIZA J0649+1801	0.064	relic	11'	...	321±46	...	-/- 9/-	...	0.49±0.07	...
CIZA J2242+5301-N	0.1921	relic(+halo)	9'	144±15	46/-/-	1.16±0.05
CIZA J2242+5301-S	0.1921	relic(+halo)	7.5'	18±2	46/-/-	0.25±0.05
Coma	0.0231	relic(+halo)	30'	260±39 ^c	47/-/-	-0.50±0.07
El Gordo-NW	0.870	relic	1'	7.0±0.5	19±2	...	0/48/-	1.33±0.03	1.77±0.05	...
MACS J1752+4440-NE	0.366	relic(+halo)	4'	65.3±3.9	...	410±33	49/-/32	1.44±0.03	...	2.23±0.04
MACS J1752+4440-SW	0.366	relic(+halo)	3'	30.2±1.8	...	163±13	49/-/32	1.10±0.03	...	1.83±0.04
PLCK G287.0+32.9-NW	0.39	relic(+halo)	4.5'	27±4 ^c	110±11 ^c	216±32 ^c	0/36/36	1.12±0.07	1.73±0.05	2.02±0.07
PLCK G287.0+32.9-SE	0.39	relic(+halo)	3.5'	10±2 ^c	50±5 ^c	114±17 ^c	0/36/36	0.68±0.10	1.38±0.05	1.60±0.07
PSZ1 G096.9+24.2-N	0.3	relic	3.3'	8.9±0.8	50/-/-	0.38±0.21
PSZ1 G096.9+24.2-S	0.3	relic	5.3'	18.3±1.9	50/-/-	0.69±0.05
RXC J1053+5452	0.0704	relic	7.5'	15±2	9/-/-	-0.75±0.06
RXC J1314-2515-E	0.2439	relic(+halo)	2.5'	10.1±0.3	28.0±1.4	52±4	51/2/1	0.23±0.01	0.69±0.02	0.94±0.03
RXC J1314-2515-W	0.2439	relic(+halo)	4.5'	20.2±0.5	64.8±3.2	137±11	51/2/1	0.53±0.01	1.04±0.02	1.36±0.04
Toothbrush	0.225	relic	8.5'	319.5±20.8	797±52	1600±100	39/39/59	1.65±0.03	2.05±0.03	2.35±0.03
Z5247	0.229	relic(+halo)	3'	3.1±0.2	9.3±1.0	23.1±2.5	40/40/0	-0.34±0.03	0.13±0.05	0.53±0.05
ZwCl0008+5215-E	0.1032	relic	12'	56.0±3.5	230±25	545±59	52/52/0	0.17±0.03	0.78±0.05	1.16±0.05
ZwCl0008+5215-W	0.1032	relic	2.5'	11.0±1.2	56±8	89±13	52/52/0	-0.54±0.05	0.17±0.07	0.37±0.07
ZwCl2341+0000-N	0.27	relic	1'	...	14±3	18±4	-/53/0	...	0.47±0.10	0.58±0.11
ZwCl2341+0000-S	0.27	relic	5'	...	37±13	58±20	-/53/0	...	0.89±0.19	1.09±0.18
A478	0.088	mini-halo	3'	16.6±3	54/-/-	-0.50±0.09
A1835	0.2532	mini-halo	2'	6.1±1.3	54/-/-	0.05±0.10
A2029	0.0765	mini-halo	6'	19.5±2.5	54/-/-	-0.56±0.06
A2204	0.152	mini-halo	0.6'	8.6±0.9	54/-/-	-0.29±0.05
A2390	0.228	mini-halo	2'	28.3±4.3	54/-/-	0.61±0.07
A3444	0.254	mini-halo	0.5'	...	29.5±0.5	...	-/40/-	...	0.74±0.01	...
2A0335	0.0347	mini-halo	3.5'	21.1±2.1	54/-/-	-1.23±0.05
MS 1455+2232	0.2578	mini-halo	2'	8.5±1.1	54/-/-	0.21±0.06
Ophiuchus	0.028	mini-halo	15'	83.4±6.6	54/-/-	-0.83±0.04
Perseus	0.0179	mini-halo	12'	3020±153	54/-/-	0.34±0.02
Phoenix	0.596	mini-halo	1'	...	17±5	...	-/55/-	...	1.34±0.15	...
RBS797	0.35	mini-halo	1'	5.2±0.6	54/-/-	0.29±0.05
RXC J1504-0248	0.2153	mini-halo	1'	20.0±1.0	59±3	121±6	54/40/56	0.41±0.02	0.88±0.02	1.19±0.02
RXC J1532+3021	0.3621	mini-halo	0.7'	7.5±0.4	16±1	33.5±4.4	54/54/54	0.49±0.02	0.81±0.03	1.14±0.06
RX J1347-1145	0.4516	mini-halo	2'	34.1±2.3	54/-/-	1.36±0.03
RX J1720+2638	0.1644	mini-halo	1.5'	68±5	170±12	365±58	57/57/57	0.69±0.03	1.08±0.03	1.41±0.08
RX J2129+0005	0.235	mini-halo	1'	2.4±0.4 ^c	8±1	...	40/40/-	-0.43±0.08	0.09±0.06	...
S780	0.236	mini-halo	0.5'	...	35±9	...	-/40/-	...	0.74±0.13	...
Z3146	0.290	mini-halo	1'	5.2±0.8 ^c	54/-/-	0.11±0.07

Notes: Columns: (1) cluster name; (2) redshift; (3) type of diffuse radio emission—halos, relics, or mini-halos. Known “radio Phoenix” looks like it is from a radio galaxy and is not included in this table; (4) angular size; (5)–(7) flux of halos, relics, and mini-halos at 1.4 GHz, 610 MHz, and 325 MHz, all in mJy; (8) reference numbers of these radio fluxes; (9)–(11) radio power (in 10^{24} W/Hz) at these three frequencies after the k -correction.

Notes for some measurements are:

^a Calculated from fluxes of whole emission region minus relic region.

^b Estimated from flux at a nearby frequency.

^c Uncertainty assumed to be 15%.

References. 0—estimated by us based on measurements available at other frequencies; 1—Venturi et al. (2013); 2—Venturi et al. (2008); 3—Murgia et al. (2010); 4—Vacca et al. (2014); 5—Dallacasa et al. (2009); 6—Brunetti et al. (2008); 7—Bacchi et al. (2003); 8—Giovannini & Feretti (2000); 9—van Weeren et al. (2011b); 10—Macario et al. (2010); 11—Macario et al. (2011); 12—Govoni et al. (2001); 13—Giacintucci et al. (2009b); 14—Vacca et al. (2011); 15—Giovannini et al. (2009); 16—Drabent et al. (2015); 17—Feretti et al. (2001); 18—Feretti et al. (2004); 19—Govoni et al. (2005); 20—Pizzo & de Bruyn (2009); 21—Clarke & Ensslin (2006); 22—Brentjens (2008); 23—Storm et al. (2015); 24—Venturi et al. (2003); 25—Giacintucci et al. (2005); 26—Shimwell et al. (2014); 27—Brown et al. (2011); 28—Bonafede et al. (2014b); 29—Kim et al. (1990); 30—Giovannini et al. (1993); 31—Venturi et al. (1990); 32—Bonafede et al. (2012); 33—Bonafede et al. (2009b); 34—Pandey-Pommier et al. (2013); 35—Giacintucci et al. (2013); 36—Bonafede et al. (2014a); 37—Giacintucci et al. (2011a); 38—Giacintucci et al. (2009a); 39—van Weeren et al. (2012b); 40—Kale et al. et al. (2015); 41—Giacintucci et al. et al. (2008); 42—Bonafede et al. (2009a); 43—Trasatti et al. (2015); 44—Kale et al. (2012); 45—Riseley et al. (2015); 46—van Weeren et al. (2011a); 47—Giovannini et al. (1991); 48—Lindner et al. (2014); 49—van Weeren et al. (2012a); 50—de Gasperin et al. (2014); 51—Feretti et al. (2005); 52—van Weeren et al. (2011c); 53—van Weeren et al. (2009); 54—Giacintucci et al. (2014b); 55—van Weeren et al. (2014); 56—Giacintucci et al. (2011b); 57—Giacintucci et al. (2014a).

TABLE 2
MASSES, MASS PROXIES, AND DYNAMICAL PARAMETERS FOR 75 GALAXY CLUSTERS

Name (1)	$\log L_X$ (2)	$\log L_{500}$ (3)	$\log M_{\text{SZ}, 500}$ (4)	$\log M_{500}$ (5)	References (6)	Γ (7)	$\log c$ (8)	$\log \omega$ (9)	$\log(P_3/P_0)$ (10)	References (11)
A115	0.96±0.12	0.87±0.12	0.88±0.02	...	1/ 2/ 3/ -	-0.76±0.11	-0.49±0.01	-2.34±0.07	-6.06±0.06	28/ 0/ 0/ 0
A209	0.80±0.05	0.88±0.01	0.93±0.02	1.03±0.07	4/ 5/ 3/ 6	-0.24±0.11	-0.72±0.02	-1.60±0.02	-7.27±0.54	0/ 29/ 0/ 0
A399	0.59±0.06	0.26±0.01	0.72±0.02	0.76±0.02	1/ 7/ 3/ 6	0.13±0.05	0/ -/ -/ -
A478	0.87±0.02	1.01±0.01	0.84±0.02	0.91±0.02	8/ 7/ 3/ 6	-/ -/ -/ -
A520	0.95±0.11	0.89±0.01	0.89±0.02	1.01±0.06	1/ 5/ 3/ 6	-0.27±0.06	-1.04±0.01	-0.80±0.01	-6.05±0.03	0/ 29/ 0/ 0
A521	0.91±0.08	0.92±0.01	0.86±0.03	0.99±0.07	4/ 5/ 3/ 6	...	-1.01±0.02	-1.12±0.01	-5.87±0.26	-29/ 0/ 0
A545	0.75±0.04	0.80±0.01	0.73±0.03	...	4/ 5/ 3/ -	-0.35±0.04	0/ -/ -/ -
A665	0.99±0.07	0.92±0.01	0.95±0.02	1.04±0.07	1/ 5/ 3/ 6	-0.26±0.10	-0.76±0.01	-1.11±0.01	-6.48±0.03	28/ 0/ 0/ 0
A697	1.02±0.08	1.11±0.01	1.04±0.01	1.16±0.08	9/ 5/ 3/ 6	-0.22±0.06	-0.82±0.02	-1.93±0.09	-6.77±0.30	28/29/ 0/ 0
A746	0.57±0.15*	0.53±0.15	0.73±0.03	...	10/ 0/ 3/ -	-2.49±0.10	0/ -/ -/ -
A754	0.63±0.01	0.27±0.01	0.84±0.01	0.84±0.02	4/ 7/ 3/ 6	-0.17±0.11	0/ -/ -/ -
A773	0.91±0.08	0.86±0.01	0.84±0.02	0.87±0.06	1/ 5/ 3/ 6	-0.12±0.07	-0.74±0.01	-1.56±0.01	-6.97±0.09	28/29/ 0/ 0
A1240	-0.01±0.02	-0.05±0.03	11/ 0/ -/ -	-0.52±0.12	28/ -/ -/ -
A1300	1.15±0.07	1.06±0.01	0.95±0.02	1.27±0.07	4/ 5/ 3/ 6	-0.95±0.12	-0.72±0.02	-1.31±0.01	-6.07±0.08	0/ 29/ 0/ 0
A1351	0.74±0.11	0.72±0.11	0.84±0.02	...	8/ 2/ 3/ -	-1.23±0.15	-1.07±0.02	-1.18±0.01	-6.24±0.26	28/ 0/ 0/ 0
A1612	0.39±0.18	0.38±0.18	0.65±0.05	...	4/ 2/ 3/ -	-1.71±0.12	28/ -/ -/ -
A1689	1.15±0.04	1.16±0.01	0.94±0.02	0.96±0.07	4/ 7/ 3/ 6	0.47±0.05	-0.46±0.01	-2.65±0.77	-7.96±0.14	28/ 0/ 0/ 0
A1758N	1.09±0.10	0.94±0.01	0.91±0.02	...	12/ 5/ 3/ -	-0.70±0.08	-0.99±0.01	-0.84±0.01	-5.35±0.03	28/29/ 0/ 0
A1835	1.39±0.06	1.38±0.01	0.99±0.02	1.02±0.05	1/ 7/ 3/ 6	0.56±0.02	-0.43±0.02	-2.55±0.37	-8.10±0.50	28/ 0/ 0/ 0
A1914	1.03±0.04	0.98±0.01	0.86±0.02	0.96±0.07	12/ 7/ 3/ 6	-0.36±0.10	-0.65±0.01	-1.17±0.01	-6.95±0.04	28/ 0/ 0/ 0
A1995	0.95±0.06	0.78±0.01	0.69±0.03	...	8/ 5/ 3/ -	-0.09±0.07	28/ -/ -/ -
A2029	0.95±0.12	0.89±0.01	0.85±0.01	0.93±0.02	12/ 7/ 3/ 6	0.40±0.03	-0.37±0.01	-2.50±0.01	-9.28±0.54	28/ 0/ 0/ 0
A2061	0.31±0.07	0.27±0.07	0.56±0.03	...	1/ 2/ 3/ -	-0.58±0.11	28/ -/ -/ -
A2069	0.66±0.07	0.63±0.07	0.73±0.02	...	1/ 2/ 3/ -	-0.26±0.04	28/ -/ -/ -
A2163	1.36±0.03	1.40±0.02	1.21±0.01	1.41±0.02	4/ 7/ 3/ 6	-1.05±0.05	-0.90±0.02	-1.27±0.01	-6.02±0.28	0/ 29/ 0/ 0
A2204	1.14±0.02	1.20±0.01	0.89±0.02	0.98±0.02	8/ 7/ 3/ 6	0.28±0.05	-0.30±0.01	-3.24±0.60	-8.90±0.20	28/ 0/ 0/ 0
A2218	0.75±0.04	0.71±0.04	0.82±0.01	0.79±0.08	1/14/ 3/ 6	0.33±0.03	-0.73±0.01	-1.82±0.01	-6.90±0.08	0/ 0/ 0/ 0
A2219	1.10±0.05	1.23±0.01	1.07±0.01	1.21±0.06	1/ 7/ 3/ 6	-0.24±0.06	-0.86±0.01	-1.58±0.01	-6.39±0.04	0/ 29/ 0/ 0
A2255	0.42±0.02	0.70±0.05	0.73±0.01	0.71±0.08	12/ 7/ 3/ 6	-1.02±0.10	28/ -/ -/ -
A2256	0.58±0.02	0.48±0.01	0.79±0.01	0.80±0.02	12/ 7/ 3/ 6	-0.17±0.08	28/ -/ -/ -
A2319	0.87±0.02	0.19±0.03	0.94±0.01	...	13/ 7/ 3/ -	0.14±0.08	0/ -/ -/ -
A2345	0.63±0.06	0.59±0.06	0.77±0.03	...	4/ 2/ 3/ -	...	-1.17±0.04	-0.91±0.01	-5.85±0.05	-/ 0/ 0/ 0
A2390	1.13±0.12	1.30±0.01	0.99±0.01	1.11±0.06	1/ 7/ 3/ 6	0.04±0.06	-0.54±0.01	-2.38±0.21	-7.24±0.14	28/29/ 0/ 0
A2744	1.10±0.05	1.17±0.01	0.99±0.02	1.18±0.06	4/ 5/ 3/ 6	-1.03±0.04	-1.00±0.02	-1.17±0.01	-5.91±0.11	0/ 29/ 0/ 0
A3365	-0.06±0.15*	-0.10±0.15	15/ 0/ -/ -	-/ -/ -/ -
A3376	0.03±0.02	0.00±0.02	0.38±0.03	0.41±0.02	4/ 2/ 3/ 6	-/ -/ -/ -
A3444	1.14±0.04	1.08±0.04	0.87±0.02	...	4/ 2/ 3/ -	...	-0.35±0.01	-3.27±0.46	-7.53±0.03	-/ 0/ 0/ 0
A3562	0.17±0.03	0.02±0.01	0.39±0.04	0.55±0.02	4/ 7/ 3/ 6	0.29±0.04	0/ -/ -/ -
A3667	1.05±0.02	0.81±0.01	0.85±0.01	0.95±0.02	4/ 7/ 3/ 6	-/ -/ -/ -
2A0335	0.35±0.01	0.32±0.01	0.36±0.03	0.41±0.02	8/ 7/ 3/ 6	-/ -/ -/ -
Bullet	1.36±0.04	1.35±0.01	1.12±0.01	1.29±0.06	4/ 5/ 3/ 6	...	-0.90±0.01	-0.77±0.01	-5.41±0.01	-/ 0/ 0/ 0
CIZA J0649+1801	0.08±0.06	0.07±0.06	16/ 2/ -/ -	-/ -/ -/ -
CIZA J2242+5301	0.83±0.10	0.58±0.10	17/ 2/ -/ -	-/ -/ -/ -
CL0016+16	1.29±0.01	1.19±0.01	0.99±0.02	1.15±0.07	18/ 5/ 3/ 6	...	-0.85±0.01	-1.78±0.06	-6.98±0.19	-/ 0/ 0/ 0
CL0217+70	-0.20±0.15*	-0.24±0.15	19/ 0/ -/ -	-/ -/ -/ -
CL1821+64	1.16±0.01	1.12±0.01	0.83±0.02	...	20/ 0/ 3/ -	...	-0.41±0.01	-2.64±0.06	-7.21±0.08	-/ 0/ 0/ 0
Coma	0.58±0.01	0.07±0.01	0.86±0.01	...	1/ 7/ 3/ -	-0.22±0.05	0/ -/ -/ -
El Gordo	...	1.55±0.02	1.03±0.02	...	-/21/ 3/ -	...	-0.70±0.01	-0.97±0.01	-5.46±0.06	-/ 0/ 0/ 0
MACS J0553-3342	...	1.23±0.15	0.94±0.02	...	-/22/ 3/ -	...	-0.90±0.01	-0.91±0.01	-5.34±0.02	-/ 0/ 0/ 0
MACS J0717+3745	1.39±0.01	1.38±0.01	1.06±0.02	1.33±0.05	18/ 5/ 3/ 6	...	-0.96±0.02	-1.79±0.09	-5.38±0.04	-/ 0/ 0/ 0
MACS J1752+4440	0.92±0.15*	0.88±0.16	0.83±0.03	...	23/ 0/ 3/ -	-1.82±0.12	0/ -/ -/ -
MS1455+2232	0.92±0.12	0.94±0.13	8/ 2/ -/ -	0.22±0.04	-0.24±0.02	-2.43±0.18	-7.71±0.14	28/29/ 0/ 0
Ophiuchus	0.72±0.01	0.58±0.01	16/ 7/ -/ -	0.09±0.08	0/ -/ -/ -
Perseus	0.89±0.01	0.79±0.01	12/ 2/ -/ -	0.06±0.06	0/ -/ -/ -
Phoenix	0.95±0.03	...	-/ -/ 3/ -	...	-0.25±0.02	-2.63±0.64	-7.91±0.66	-/ 0/ 0/ 0
PLCK G171.9-40.7	...	1.05±0.01	1.03±0.02	...	-/ 5/ 3/ -	...	-0.83±0.01	-1.75±0.03	-6.88±0.09	-/ 0/ 0/ 0
PLCK G287.0+32.9	...	1.24±0.01	1.17±0.01	...	-/24/ 3/ -	-/ -/ -/ -
PSZ1 G096.9+24.2	0.58±0.15*	0.54±0.15	0.67±0.03	...	25/ 0/ 3/ -	-/ -/ -/ -
RBS797	1.31±0.02	1.30±0.02	0.75±0.04	0.86±0.07	26/ 2/ 3/ 6	...	-0.25±0.01	-3.44±0.23	-9.49±0.53	-/ 0/ 0/ 0
RXC J0107+5408	0.44±0.08	0.45±0.08	0.77±0.02	...	16/ 2/ 3/ -	-/ -/ -/ -

TABLE 2
continued

Name (1)	$\log L_X$ (2)	$\log L_{500}$ (3)	$\log M_{\text{SZ}, 500}$ (4)	$\log M_{500}$ (5)	References (6)	Γ (7)	$\log c$ (8)	$\log \omega$ (9)	$\log(P_3/P_0)$ (10)	References (11)
RXC J1053+5452	0.58±0.05	-0.35±0.05	9/ 2/ -/-	...	-0.91±0.01	-1.26±0.01	-6.71±0.16	-/ 0/ 0/ 0
RXC J1314-2515	1.04±0.08	1.00±0.08	0.83±0.04	...	4/ 2/ 3/ -	-0.39±0.07	0/ -/-/-
RXC J1504-0248	1.45±0.02	1.45±0.01	0.82±0.03	...	4/ 7/ 3/ -	0.32±0.04	-0.22±0.01	-2.78±1.08	-8.09±0.09	28/29/ 0/ 0
RXC J1514-1523	0.85±0.08	0.81±0.08	0.95±0.02	...	4/ 2/ 3/ -	...	-1.19±0.02	-1.25±0.01	-6.28±0.07	-/ 0/ 0/ 0
RXC J1532+3021	1.22±0.02	1.30±0.02	...	0.91±0.08	26/14/ -/ 6	0.28±0.04	-0.27±0.01	-2.97±1.28	-8.66±0.25	28/ 0/ 0/ 0
RXC J2003-2323	0.97±0.08	0.96±0.01	0.95±0.02	...	4/ 5/ 3/ -	...	-1.22±0.02	-0.73±0.01	-6.79±0.16	-/29/ 0/ 0
RX J1347-1145	1.65±0.05	1.63±0.01	1.04±0.02	1.27±0.06	4/14/ 3/ 6	...	-0.40±0.01	-1.78±0.01	-6.80±0.08	-/ 0/ 0/ 0
RX J1720+2638	0.87±0.03	0.96±0.01	0.77±0.03	...	12/ 7/ 3/ -	0.33±0.03	-0.33±0.01	-2.99±0.45	-7.81±0.14	28/ 0/ 0/ 0
RX J2129+0005	1.07±0.13	1.00±0.02	0.64±0.06	0.82±0.07	1/14/ 3/ 6	0.42±0.04	-0.40±0.01	-2.43±0.11	-7.11±0.05	28/ 0/ 0/ 0
S780	1.19±0.09	0.94±0.01	0.89±0.03	...	4/ 2/ 3/ -	...	-0.36±0.01	-2.42±0.11	-7.49±0.17	-/ 0/ 0/ 0
Toothbrush	1.00±0.09	0.96±0.09	1.03±0.02	...	27/ 0/ -/-	...	-1.03±0.01	-1.18±0.01	-6.38±0.03	-/ 0/ 0/ 0
Z3146	1.29±0.04	1.28±0.02	0.81±0.03	0.91±0.06	8/14/ -/ 6	0.39±0.02	-0.34±0.01	-2.31±0.03	-8.03±0.11	0/ 0/ 0/ 0
Z5247	0.80±0.12	0.63±0.03	0.77±0.03	0.85±0.11	1/14/ 3/ 6	-0.09±0.05	28/ -/-/-
ZwCl0008+5215	-0.30±0.12	-0.34±0.12	0.53±0.05	...	27/ 0/ 3/ -	-/ -/-/-
ZwCl2341+0000	0.39±0.09	0.35±0.09	0.71±0.04	...	25/ 0/ 3/ -	-0.56±0.08	-1.08±0.04	-0.83±0.01	-5.76±0.19	28/ 0/ 0/ 0

Notes. Columns: (1) cluster name; (2)–(5) mass proxies of cluster, L_X and L_{500} in $10^{44} \text{ erg s}^{-1}$, and cluster masses $M_{\text{SZ}, 500}$ and M_{500} in $10^{14} M_\odot$. The uncertainty with mark * for mass proxy is not available from the reference, and 30% of the total luminosity is taken here; (6) references of mass proxies or mass; (7)–(10) optical and X-ray dynamical parameters, while $\log \omega$ and $\log(P_3/P_0)$ are calculated in 500 kpc; (11) references for dynamical parameters. Clusters hosting both radio halo and relic are not listed twice.

References: 0—this paper by the authors; 1—Ebeling et al. (1998); 2—Piffaretti et al. (2011); 3—Planck Collaboration et al. (2015); 4—Böhringer et al. (2004); 5—Cassano et al. (2013); 6—Wen & Han (2015); 7—Zhao et al. (2015); 8—Böhringer et al. (2000); 9—Popesso et al. (2004); 10—van Weeren et al. (2011b); 11—David et al. (1999); 12—Ebeling et al. (1996); 13—Reiprich & Böhringer (2002); 14—Mantz et al. (2010); 15—Feretti et al. (2012); 16—Ebeling et al. (2002); 17—Kocevski et al. (2007); 18—Ebeling et al. (2007); 19—Brown et al. (2011); 20—Bonafede et al. (2014b); 21—Menanteau et al. (2012); 22—Bonafede et al. (2012); 23—Bonafede et al. (2012); 24—Bonafede et al. (2009a); 25—de Gasperin et al. (2014); 26—Ebeling et al. (2010); 27—Voges et al. (1999); 28—Wen & Han (2013); 29—Cassano et al. (2010).

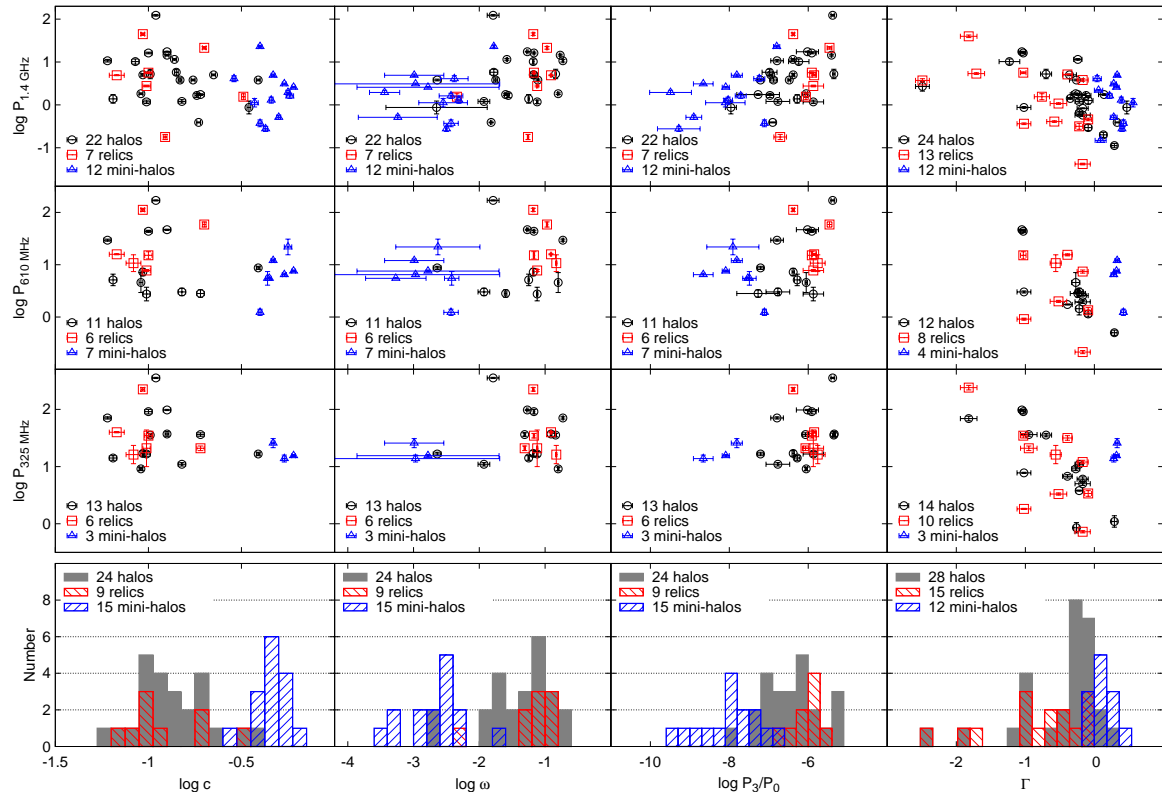


FIG. 1.— The radio power at three frequencies of radio halos (circles), relics (squares), and mini-halos (triangles) are plotted dynamic parameters of galaxy clusters (panels in the upper 3 rows), and the distributions dynamic parameters are shown in the bottom panels.

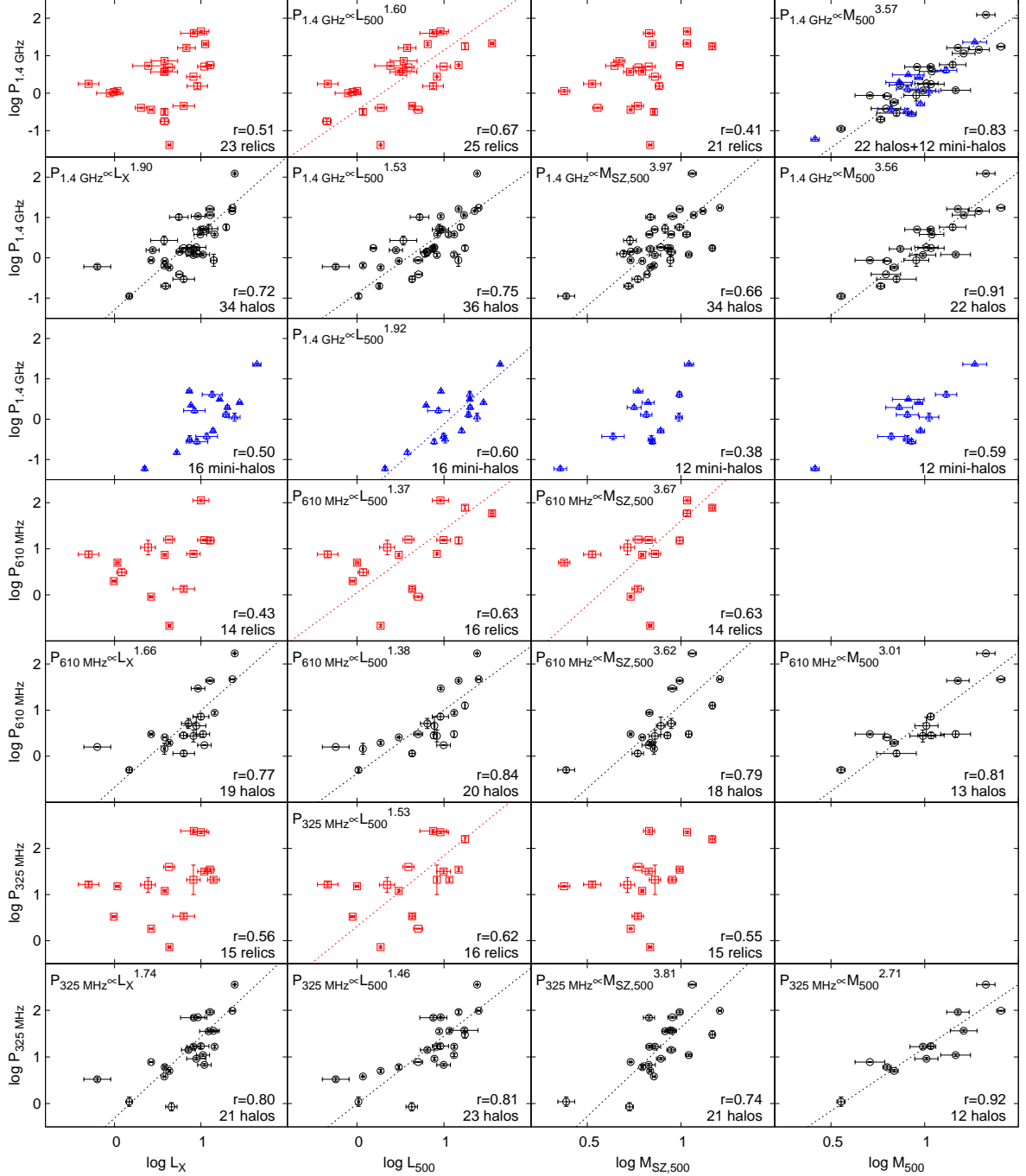


FIG. 2.— The scaling relations for radio power of radio relics and halos with cluster masses or mass proxies at three frequencies. Plots are omitted if there are only few (< 10) data points, e.g., those for mini-halos at two lower frequencies and those for relics against M_{500} . Dotted lines are the best fits, carried out only if the Spearman rank-order correlation coefficient $r \gtrsim 0.6$. The radio powers $P_{1.4 \text{ GHz}}$ of 22 halos and 12 mini-halos are plotted together in the right panel of the first row (originally for relics) to show their consistency with the scaling relations.

of circular apertures centered on the X-ray peak from R_{ap} to $0.05R_{\text{ap}}$ in steps of $0.05R_{\text{ap}}$, thus

$$\omega = \left[\frac{1}{N-1} \sum (\Delta_i - \langle \Delta \rangle)^2 \right]^{1/2} \times \frac{1}{R_{\text{ap}}}. \quad (4)$$

Here Δ_i is the distance between the X-ray peak and the centroid of the i th aperture (Poole et al. 2006). Buote & Tsai (1995) defined the power ratios as dimensionless morphological parameters from the two-dimensional multipole expansion of the projected gravitational potential of clusters inside R_{ap} .

The moments, P_m , are defined as follows:

$$P_0 = [a_0 \ln(R_{\text{ap}})]^2, \quad (5)$$

$$P_m = \frac{1}{2m^2 R_{\text{ap}}^{2m}} (a_m^2 + b_m^2). \quad (6)$$

The moments a_m and b_m are calculated using

$$a_m(R) = \int_{R' \leq R_{\text{ap}}} S(x') (R')^m \cos(m\phi') d^2x', \quad (7)$$

TABLE 3
THE SCALING RELATION FOR RADIO POWER OF RELICS, RADIO HALOS, AND MINI-HALOS IN GALAXY CLUSTERS TOGETHER WITH THE INTRINSIC DATA SCATTER σ^2/dof AND THE FITTING χ^2/dof .

Parameters	No.	Type	r	p	The Best Fitted Relations	σ^2/dof	χ^2/dof
$P_{1.4 \text{ GHz}} - L_{500}$	25	relic	0.67	0.00	$\log P_{1.4 \text{ GHz}} = (1.60 \pm 0.17) \log L_{500} - (0.46 \pm 0.24)$	0.474	0.965
$P_{610 \text{ MHz}} - L_{500}$	16	relic	0.63	0.01	$\log P_{610 \text{ MHz}} = (1.37 \pm 0.13) \log L_{500} + (0.05 \pm 0.22)$	0.478	0.983
$P_{610 \text{ MHz}} - M_{\text{SZ}, 500}$	14	relic	0.63	0.02	$\log P_{610 \text{ MHz}} = (3.67 \pm 0.20) \log M_{\text{SZ}, 500} - (2.06 \pm 0.24)$	0.615	0.988
$P_{325 \text{ MHz}} - L_{500}$	16	relic	0.62	0.01	$\log P_{325 \text{ MHz}} = (1.53 \pm 0.15) \log L_{500} + (0.31 \pm 0.23)$	0.530	0.985
$P_{1.4 \text{ GHz}} - L_X$	34	halo	0.72	0.00	$\log P_{1.4 \text{ GHz}} = (1.90 \pm 0.14) \log L_X - (1.29 \pm 0.18)$	0.250	0.868
$P_{1.4 \text{ GHz}} - L_{500}$	36	halo	0.75	0.00	$\log P_{1.4 \text{ GHz}} = (1.53 \pm 0.13) \log L_{500} - (0.88 \pm 0.18)$	0.226	0.949
$P_{1.4 \text{ GHz}} - M_{\text{SZ}, 500}$	34	halo	0.66	0.00	$\log P_{1.4 \text{ GHz}} = (3.97 \pm 0.18) \log M_{\text{SZ}, 500} - (3.18 \pm 0.20)$	0.263	0.969
$P_{1.4 \text{ GHz}} - M_{500}$	22	halo	0.91	0.00	$\log P_{1.4 \text{ GHz}} = (3.56 \pm 0.12) \log M_{500} - (3.21 \pm 0.15)$	0.139	0.746
$P_{610 \text{ MHz}} - L_X$	19	halo	0.77	0.00	$\log P_{610 \text{ MHz}} = (1.66 \pm 0.13) \log L_X - (0.67 \pm 0.17)$	0.246	0.904
$P_{610 \text{ MHz}} - L_{500}$	20	halo	0.84	0.00	$\log P_{610 \text{ MHz}} = (1.38 \pm 0.12) \log L_{500} - (0.38 \pm 0.16)$	0.206	0.965
$P_{610 \text{ MHz}} - M_{\text{SZ}, 500}$	18	halo	0.79	0.00	$\log P_{610 \text{ MHz}} = (3.62 \pm 0.16) \log M_{\text{SZ}, 500} - (2.50 \pm 0.17)$	0.241	0.983
$P_{610 \text{ MHz}} - M_{500}$	13	halo	0.81	0.00	$\log P_{610 \text{ MHz}} = (3.01 \pm 0.11) \log M_{500} - (2.27 \pm 0.14)$	0.165	0.823
$P_{325 \text{ MHz}} - L_X$	21	halo	0.80	0.00	$\log P_{325 \text{ MHz}} = (1.74 \pm 0.12) \log L_X - (0.31 \pm 0.15)$	0.229	0.873
$P_{325 \text{ MHz}} - L_{500}$	23	halo	0.81	0.00	$\log P_{325 \text{ MHz}} = (1.46 \pm 0.11) \log L_{500} - (0.01 \pm 0.15)$	0.198	0.926
$P_{325 \text{ MHz}} - M_{\text{SZ}, 500}$	21	halo	0.74	0.00	$\log P_{325 \text{ MHz}} = (3.81 \pm 0.16) \log M_{\text{SZ}, 500} - (2.18 \pm 0.17)$	0.240	0.963
$P_{325 \text{ MHz}} - M_{500}$	12	halo	0.92	0.00	$\log P_{325 \text{ MHz}} = (2.71 \pm 0.07) \log M_{500} - (1.52 \pm 0.09)$	0.111	0.789
$P_{1.4 \text{ GHz}} - L_{500}$	16	mini-halo	0.60	0.01	$\log P_{1.4 \text{ GHz}} = (1.92 \pm 0.10) \log L_{500} - (2.03 \pm 0.15)$	0.211	0.989

and

$$b_m(R) = \int_{R' \leq R_{\text{ap}}} S(x')(R')^m \sin(m\phi') d^2x', \quad (8)$$

where $S(x)$ is the X-ray surface brightness of the pixel labeled x . P_3/P_0 is the power ratio, which was found to be related to substructures (e.g., Böhringer et al. 2010; Cassano et al. 2010). We therefore also take P_3/P_0 as another dynamical parameter of clusters.

The dynamical parameters in Table 2 are taken directly from the literature for the galaxy clusters that have diffuse radio emission. For 49 clusters, we derive the concentration parameters, c , the centroid shifts, ω , and the power ratios, P_3/P_0 , from the *Chandra* 0.5–5 keV band X-ray images¹ by using Equations (3)–(8). We take our newly derived dynamical parameters if they are different from the values given in the literature.

3. THE SCALING RELATIONS FOR RADIO POWER AND THE FUNDAMENTAL PLANE IN THE 3D PARAMETER SPACE

The data distribution of the three sets of parameters is shown in Figure 1. In general, the values of radio power for the three types of diffuse emission in galaxy clusters are in the same range of magnitude.

The ranges of dynamical parameters for clusters with radio halos and mini-halos in Figure 1 are consistent with those of Cassano et al. (2010, Figure 1). In particular, we found that galaxy clusters with mini-halos have very large c and Γ ($\log c \gtrsim -0.5$, $\Gamma \gtrsim -0.2$) and a small ω and P_3/P_0 ($\log \omega \lesssim -2$, $\log(P_3/P_0) \lesssim -7$), indicating the relaxed state of these clusters. Clusters with relics and halos share quite similar dynamical properties. The Γ distributions show clusters with relics to be more disturbed than clusters with radio halos, which is probably related to the fact that radio relics are likely found in clusters characterized by mergers happening almost on the plane of the sky.

Clusters with relics have a slightly wider range of X-ray luminosity and hence a larger range of masses than those with

halos (see Figure 2), while clusters with radio mini-halos have a slightly smaller range of higher X-ray luminosity.

In the following we discuss the scaling relations in the two-dimensional data distributions for the radio power, and then try to find the fundamental plane in three-dimensional parameter spaces. The Bivariate Correlated Errors and intrinsic Scatter (BCES) method has previously been used in similar analyses (e.g., Brunetti et al. 2009; Cassano et al. 2013). We develop the BCES-Reduced Major Axis (BCES-RMA) method for the three-dimensional data fitting (see the appendix for details), and use the BCES-RMA in the following to get the regression parameters for 2D and 3D fittings. The unified deviations σ^2/dof for the intrinsic scatter (see Equation (A11) in the appendix, not including the contribution from measurement uncertainties) as well as the fitting χ^2/dof (see Equation (A13) in the appendix) are calculated accordingly. In addition, we use the Spearman rank-order correlation coefficient, r , to assess data correlations and the probability of the null hypothesis p to indicate the reliability of correlations (see Press et al. 1992, p. 634). For 3D fittings, we first compute \hat{z}_i from variables x_i and y_i based on the 3D best fitting relations, and then calculate the coefficient r from \hat{z}_i and variables z_i .

3.1. The Scaling Relations between Radio Power and Cluster Mass

The scaling relation between radio power of radio halos and mass proxies of galaxy clusters has been studied by many authors, e.g., Liang et al. (2000), Brunetti et al. (2009), Basu (2012), and Cassano et al. (2013). This relation can be written as

$$\log P_{1.4 \text{ GHz}} = \alpha \log M + C, \quad (9)$$

where C is the normalization factor, M is the mass parameter of clusters, and α is the index. Brunetti et al. (2009) took the X-ray luminosity L_X as the mass proxy for clusters and obtained $\alpha_{L_X} = 2.06 \pm 0.20$ for 22 halos and two mini-halos. Cassano et al. (2013) obtained L_{500} from the *Chandra* images for 25 clusters with halos and found $\alpha_{L_{500}} = 2.11 \pm 0.20$. By using the SZ parameter Y_{500} as a mass proxy, they obtained $\alpha_{Y_{500}} = 2.02 \pm 0.28$ for these clusters, and then found

¹ <http://cda.harvard.edu/chaser/>

TABLE 4

SEARCHING FOR A FUNDAMENTAL PLANE IN 3D PARAMETER SPACE BY INVOLVING DYNAMICAL PARAMETERS AND COMPARING THE INTRINSIC DATA SCATTER σ^2/dof AND THE FITTING χ^2/dof .

Parameters	No.	Type	r	p	The best-fitted relation	σ^2/dof	χ^2/dof
$P_{1.4 \text{ GHz}} - L_{500}$	13	halo	0.52	0.07	$\log P_{1.4 \text{ GHz}} = (2.56 \pm 0.11) \log L_{500} - (2.03 \pm 0.15)$	0.309	0.903
$P_{1.4 \text{ GHz}} - L_{500} - \Gamma$	13	halo	0.54	0.06	$\log P_{1.4 \text{ GHz}} = (1.03 \pm 0.05) \log L_{500} - (0.87 \pm 0.17) \Gamma - (0.83 \pm 0.06)$	0.050	1.002
$P_{1.4 \text{ GHz}} - L_{500} - c$	13	halo	0.64	0.02	$\log P_{1.4 \text{ GHz}} = (1.86 \pm 0.08) \log L_{500} - (2.39 \pm 0.16) \log c - (3.30 \pm 0.10)$	0.154	0.989
$P_{1.4 \text{ GHz}} - L_{500} - \omega$	13	halo	0.63	0.02	$\log P_{1.4 \text{ GHz}} = (2.05 \pm 0.06) \log L_{500} + (1.00 \pm 0.07) \log \omega - (0.07 \pm 0.07)$	0.143	0.854
$P_{1.4 \text{ GHz}} - L_{500} - \frac{P_3}{P_0}$	13	halo	0.68	0.00	$\log P_{1.4 \text{ GHz}} = (1.57 \pm 0.08) \log L_{500} + (0.61 \pm 0.01) \log \frac{P_3}{P_0} + (2.99 \pm 0.09)$	0.160	0.864
$P_{1.4 \text{ GHz}} - L_{500}$	24	halo	0.70	0.00	$\log P_{1.4 \text{ GHz}} = (1.56 \pm 0.13) \log L_{500} - (0.94 \pm 0.16)$	0.212	0.955
$P_{1.4 \text{ GHz}} - L_{500} - \Gamma$	24	halo	0.75	0.00	$\log P_{1.4 \text{ GHz}} = (1.07 \pm 0.13) \log L_{500} - (0.52 \pm 0.29) \Gamma - (0.78 \pm 0.13)$	0.130	0.955
$P_{1.4 \text{ GHz}} - M_{\text{SZ}, 500}$	24	halo	0.64	0.00	$\log P_{1.4 \text{ GHz}} = (3.69 \pm 0.16) \log M_{\text{SZ}, 500} - (2.94 \pm 0.16)$	0.209	0.958
$P_{1.4 \text{ GHz}} - M_{\text{SZ}, 500} - \Gamma$	24	halo	0.68	0.00	$\log P_{1.4 \text{ GHz}} = (2.68 \pm 0.13) \log M_{\text{SZ}, 500} - (0.55 \pm 0.28) \Gamma - (2.28 \pm 0.12)$	0.113	0.946
$P_{1.4 \text{ GHz}} - M_{500}$	17	halo	0.88	0.00	$\log P_{1.4 \text{ GHz}} = (3.19 \pm 0.10) \log L_{500} - (2.87 \pm 0.12)$	0.125	0.734
$P_{1.4 \text{ GHz}} - M_{500} - \Gamma$	17	halo	0.90	0.00	$\log P_{1.4 \text{ GHz}} = (1.75 \pm 0.12) \log L_{500} - (0.43 \pm 0.11) \Gamma - (1.61 \pm 0.10)$	0.090	0.871
$P_{1.4 \text{ GHz}} - L_{500}$	13	relic	0.62	0.02	$\log P_{1.4 \text{ GHz}} = (2.18 \pm 0.16) \log L_{500} - (1.05 \pm 0.22)$	0.626	0.947
$P_{1.4 \text{ GHz}} - L_{500} - \Gamma$	13	relic	0.71	0.01	$\log P_{1.4 \text{ GHz}} = (0.88 \pm 0.25) \log L_{500} - (0.45 \pm 0.13) \Gamma - (0.71 \pm 0.16)$	0.353	0.984
$P_{1.4 \text{ GHz}} - L_{500}$	12	mini-halo	0.48	0.11	$\log P_{1.4 \text{ GHz}} = (2.31 \pm 0.08) \log L_{500} - (2.58 \pm 0.12)$	0.230	0.960
$P_{1.4 \text{ GHz}} - L_{500} - \frac{P_3}{P_0}$	12	mini-halo	0.66	0.02	$\log P_{1.4 \text{ GHz}} = (1.37 \pm 0.08) \log L_{500} + (0.32 \pm 0.01) \log \frac{P_3}{P_0} + (1.14 \pm 0.10)$	0.172	0.964

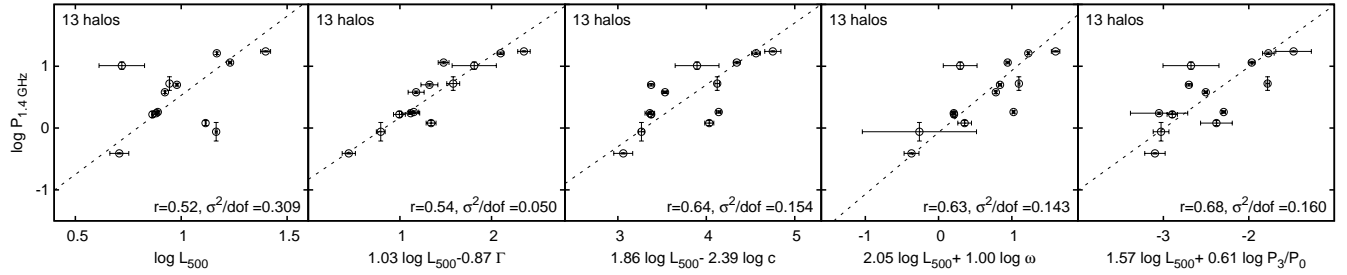


FIG. 3.— Comparison of the effectiveness by involving different dynamical parameters to reduce the data scatter.

$\alpha_{M_{500}} = 3.70 \pm 0.56$ for M_{500} . Since cluster mass M_{500} is related to L_{500} by $L_{500} \propto M_{500}^{1.64}$ (Piffaretti et al. 2011), it is understandable that $\alpha_{M_{500}} = \alpha_{L_{500}} \times 1.64$.

By using the radio power values of halos, relics, and mini-halos at the three frequencies in Table 1 and cluster masses or proxies in Table 2, we check the scaling relations between the radio power and cluster masses for galaxy clusters. The power values of a pair of relics detected from one cluster are added for the following discussions. Results are shown in Figure 2 and listed in Table 3.

First of all, let us look at different types of radio emission. The power of radio halos at any frequency is clearly correlated with the kinds of cluster masses or mass proxies. They show the strongest correlations and much less intrinsic data scattered around the best-fit correlations. For the relics and mini-halos, the radio power is found to be only marginally correlated with L_{500} (and also with $M_{\text{SZ}, 500}$ for relics at 610 MHz), and the correlations are less strong and also the points are clearly more scattered around the best-fit correlations, as shown by the σ^2/dof in Table 3. The radio power of mini-halos at 1.4 GHz, if plotted against cluster mass, is consistent with the result in Giacintucci et al. (2014b), but we find a marginal correlation between $P_{1.4 \text{ GHz}}$ and L_{500} or M_{500} with a Spearman rank-order correlation coefficient $r = 0.6$ or 0.59 . We also noticed that the radio power $P_{1.4 \text{ GHz}}$ of halos and mini-halos at 1.4 GHz can be scaled together very well with M_{500} , as shown in the right panel of the first row in Fig. 2 for the 22 halos together with 12 mini-halos.

Second, which of the mass estimates or mass proxies is good for the scaling relations? For relics and mini-halos, L_{500}

seems to be the best, because not only are more data available for the host clusters but also the other masses or proxies do not show significant correlation. For radio halos, the M_{500} estimated from gas mass is the best for the scaling relations with radio power at any frequency, though fewer data are available for host clusters and thus we cannot exclude that the small size of the sample can affect the strength of the correlation. Among the other three mass proxies, L_{500} shows a slightly better correlation with the halo radio power than L_X and $M_{\text{SZ}, 500}$, as indicated by a slightly larger Spearman rank-order correlation coefficient r and a smaller deviation σ^2/dof as listed in Table 3. Therefore L_{500} is a common mass proxy for galaxy clusters which can be scaled with the radio power of all three types of diffuse radio emission.

We noticed that at any of these three frequencies, the scaling indices $\alpha_{L_{500}}$ between the radio power and proxy L_{500} are almost the same for the relics and radio halos, though relic data are more scattered around the fitted lines. The scaling index we obtained for $P_{1.4 \text{ GHz}}$ of halos and L_X is $\alpha_{L_X} = 1.90 \pm 0.14$, which is consistent with the previous results around $\alpha_{L_X} = 2.06 \pm 0.2$ in Brunetti et al. (2009). Our scaling indices for the power of radio halos $P_{1.4 \text{ GHz}}$ against the SZ mass and M_{500} are 3.97 ± 0.18 and 3.56 ± 0.12 , respectively, which are consistent with the result $\alpha_{M_{500}} = 3.70 \pm 0.56$ obtained by Cassano et al. (2013). For relics, the scaling index we found for $P_{1.4 \text{ GHz}}$ and L_{500} is $\alpha_{L_{500}} = 1.60 \pm 0.17$, which is very consistent with the most recent result $\alpha_{M_{500}} = 2.83 \pm 0.39$ given by de Gasperin et al. (2014) if we consider $\alpha_{M_{500}} = \alpha_{L_{500}} \times 1.64$. The scaling indices $\alpha_{L_{500}}$ are roughly consistent at three frequencies if

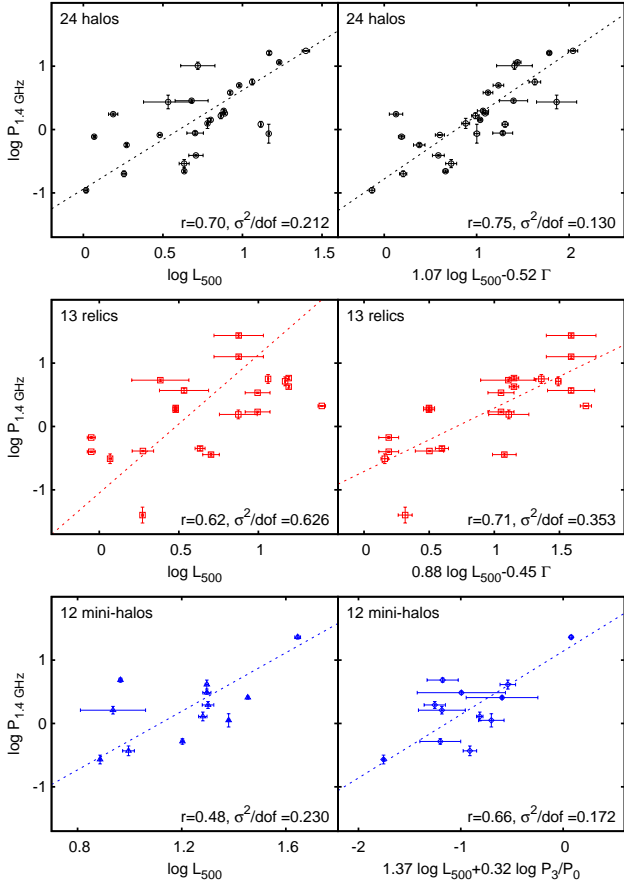


FIG. 4.— The data scatter is effectively reduced by involving dynamical parameters Γ for radio halos and relics, and P_3/P_0 for mini-halos.

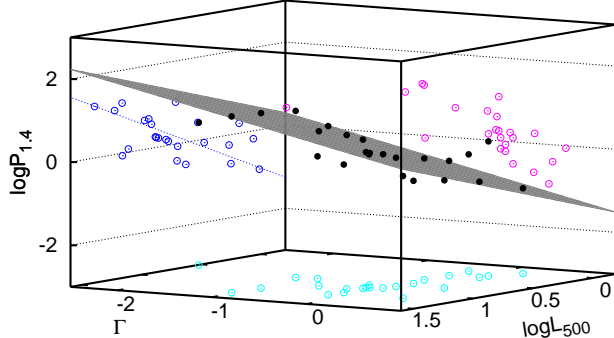


FIG. 5.— The best-fitted plane for 24 radio halos in 3D parameter space: $\log P_{1.4 \text{ GHz}} = (1.07 \pm 0.13) \log L_{500} - (0.52 \pm 0.29) \Gamma - (0.78 \pm 0.13)$. Data are projected onto the three planes and shown as open circles.

considering the uncertainties, while scaling indices $\alpha_{M_{500}}$ are different at three frequencies for the radio halos, which may be due to selection effect of the small sample and needs to be verified further in future.

3.2. Searching for the Fundamental Plane in the 3D Parameter Space

We search here for the correlation between the radio power P of halos, relics, and mini-halos with cluster mass M and the dynamical parameter D in 3D parameter spaces. Based on Equation (9), the 3D relations in general can be written as

$$\log P = \alpha \log M + \beta \log D + \gamma, \quad (10)$$

which is the fundamental plane in the 3D space. The new fitting method introduced in the appendix can fit data with uncertainties. The data scatter σ^2/dof can be calculated via the offsets from the plane by considering the data uncertainties (see the appendix).

We search for the fundamental planes separately for radio halos, mini-halos, and relics. Because there is much less data for radio power at 610 and 325 MHz, we fit here only the data of $P_{1.4 \text{ GHz}}$. We adopt L_{500} as the main mass proxy, since its values are available for most galaxy clusters. To make a reasonable comparison of data scatter among the 2D and 3D correlations, we use the same cluster subsamples to check whether the inclusion of any dynamical parameter can reduce the data scatter and improve the fit.

First of all, we check which one of the four kinds of dynamical parameters is most effective. For a subsample of 13 galaxy clusters with radio halos, all four kinds of dynamical parameters, Γ , ω , c , and P_3/P_0 , are available (as listed in Table 2). We find that involving any one of these dynamical parameters can reduce the σ^2/dof of the fitting, as listed in Table 4 and shown in Figure 3. Nevertheless the Γ can reduce the σ^2/dof most significantly from 0.309 to 0.050. In fact, the dynamical parameter Γ is available for a subsample of 24 galaxy clusters with radio halos, which works effectively as shown in Figure 4. The best fitting plane for the 24 radio halos is shown in Figure 5 in the 3D space of $P_{1.4 \text{ GHz}} - L_{500} - \Gamma$. For this subsample of 24 galaxy clusters with radio halos, the SZ mass estimates $M_{\text{SZ}, 500}$ are available. We found that if we replace L_{500} with $M_{\text{SZ}, 500}$, Γ works similarly well in the 3D fitting, see Table 4. This is also true for another subsample of 17 galaxy clusters with M_{500} .

We found that the dynamical parameter Γ also works well to reduce the data scatter for also a subsample of 13 galaxy clusters with relics, as seen in Table 4 and Figure 3. However, for a subsample of 12 galaxy clusters with mini-halos, the most effective dynamical parameter is P_3/P_0 which picks up the presence of a cold front in the X-ray images of cool-core clusters as a signature of gas sloshing (e.g., Mazzotta & Giacintucci 2008).

4. CONCLUSIONS AND DISCUSSIONS

In this paper, we collect the observed fluxes of radio halos, relics, and mini-halos of galaxy clusters from the literature and calculate the radio power of these three types of diffuse radio emission at three frequencies, $P_{1.4 \text{ GHz}}$, $P_{610 \text{ MHz}}$, and $P_{325 \text{ MHz}}$. We also collect the mass estimates and mass proxies, L_X , L_{500} , $M_{\text{SZ}, 500}$, and M_{500} for these galaxy clusters, and obtain their dynamical parameters, Γ , c , ω , and P_3/P_0 from optical and X-ray image data. The data show that galaxy clusters with relics, radio halos, and mini-halos are in different dynamical states described by dynamical parameters. Radio relics and halos are detected from merging clusters, and mini-halos from relaxed clusters. By using these data, we studied the scaling relations for relics, radio halos, and mini-halos and searched for the fundamental plane in the 3D parameter space.

We conclude from our data that the radio powers of relics, radio halos, and mini-halos are all correlated with mass proxies L_{500} . The power of radio halos shows the strongest correlations. For the relics and mini-halos the correlations are less strong and also the points are clearly more scattered around the best-fit correlations. For radio halos, the scaling indices between the radio power and the mass proxies L_{500} and $M_{\text{SZ}, 500}$ are consistent with each other at three frequen-

cies. The powers of radio halos and mini-halos can be scaled together nicely with the cluster mass M_{500} .

We found that when any of various dynamical parameters is involved, the data scatter of the scaling relations between the radio power and mass proxies can be significantly reduced. For radio halos and relics, the most effective is to include the dynamical parameter Γ derived from the optical brightness distribution of cluster member galaxies. For the mini-halos, the radio power is closely related to P_3/P_0 derived for the inner X-ray substructures of globally relaxed clusters.

Evidently the properties of diffuse radio emission in galaxy clusters are related not only to cluster mass but also to the dynamic states. First of all, to host diffuse radio emission, a galaxy cluster has to be massive enough to contain enough intracluster medium for dynamical stirring either in the central region of relaxed clusters for mini-halos or on cluster scales of merging clusters for radio halos or relics. When a massive cluster appears to be very relaxed with a cool core, a mini-halo could be produced as long as the substructures of cold fronts in the X-ray image appear (Mazzotta & Giacintucci 2008), indicating that the turbulence generated by the gas sloshing of the dark-matter cores in the cluster potential well (e.g., ZuHone et al. 2013) is responsible for re-accelerating the relativistic electrons for diffuse radio emission.

Merging of galaxy clusters can generate turbulence on a cluster scale, which can re-accelerate relativistic particles and produce Mpc-size radio halos (e.g., Brunetti & Jones 2014). The dynamical states of merging clusters can be imprinted by substructures in the hot gas distribution seen in X-ray images or by the unrelaxed velocity distribution of member galaxies or their irregular brightness distributions. Looking at two proposed theoretical models for cluster halos: (1) the secondary model in which the relativistic electrons for synchrotron emis-

sion are the secondary products of the inelastic collision of thermal protons and cosmic-ray protons in clusters, and (2) the re-acceleration model in which the relativistic electrons are re-accelerated by turbulence in the intracluster medium, we found that our results show the close relation between the dynamic stirring and radio halos in the format of a fundamental plane, which no doubt supports the re-acceleration scenario.

The merging of two massive clusters can also induce peripheral shocks that re-accelerate particles and compress or amplify the magnetic fields, so that giant radio relics can be produced in the shock region of the cluster periphery (e.g., Hoeft & Brüggen 2007; Kang & Ryu 2013). The sky distribution of member galaxy brightness is physically related to the dynamics of merging clusters, which has influence on the re-acceleration of particles in the peripheral shock regions and consequently is related to the radio power of relics as revealed in this paper.

In summary, in addition to the known scaling relations between the radio power and X-ray luminosity, we found that the power of radio halos and relics is correlated with cluster mass proxies and dynamical parameters in the form of a fundamental plane.

We thank Dr. Tiziana Venturi and also the referee for very careful reading of the manuscript and very instructive comments that helped us to improve the paper significantly. The authors are supported by the Strategic Priority Research Program “The Emergence of Cosmological Structures” of the Chinese Academy of Sciences, Grant No. XDB09010200, and the National Natural Science Foundation of China (11103032, 11473034) and the Young Researcher Grant of National Astronomical Observatories, Chinese Academy of Sciences.

APPENDIX

THE 3D LINEAR REGRESSION FOR DATA WITH UNCERTAINTIES

Linear regression analysis is widely used to study the correlation of two sets of data. Astronomical data sets usually have measurement uncertainties. The BCES method has been used for astronomical data analysis (e.g., Brunetti et al. 2009; Cassano et al. 2013; Zhao et al. 2013) because: (1) observational data have uncertainties; (2) uncertainties of data sets can be dependent; (3) regression lines such as the bisector and the orthogonal regression (OR) can be obtained easily. See Akritas & Bershady (1996) for details.

In this work, the data sets of galaxy clusters in Tables 1 and 2 have measurement uncertainties, and the level of uncertainties for different parameters obtained from different observations can be very different. For example, the uncertainty of L_{500} from Cassano et al. (2013) derived from the *Chandra* data is about a magnitude smaller than those in the MCXC catalog derived from the *ROSAT* data. The BCES method can be used to fit data in five approaches: (1) BCES($Y|X$), where the deviations of data to the fitted line are measured vertically; (2) BCES($X|Y$), where the deviations are measured horizontally; (3) OR, where the deviations are measured perpendicularly to the fitted line; (4) RMA, where the deviations are measured both perpendicularly and horizontally; (5) BCES bisector, which is the bisector of the BCES($Y|X$) and BCES($X|Y$) lines. The last three approaches are usually recommended because both axes are considered simultaneously. The BCES bisector method has not yet be developed for 3D fitting. The BCES-RMA method usually gives very similar fitting coefficients to the BCES bisector method.

The 2D BCES-RMA method is derived directly from the ordinary least-square (OLS) method, which ensures that the sum of deviations between the data points and the fitted line is as small as possible (e.g., Isobe et al. 1990). The OLS method is only available for data fitting without considering data uncertainty. If the variables of interest are denoted by X_{1i}, X_{2i} and the observed data for them denoted by Y_{1i}, Y_{2i} , we have

$$Y_{1i} = X_{1i} \pm \epsilon_{1i}, Y_{2i} = X_{2i} \pm \epsilon_{2i} \quad (\text{A1})$$

where $\epsilon_{1i}, \epsilon_{2i}$ are uncertainties. The linear regression model is formulized as

$$X_{2i} = \alpha X_{1i} + \beta. \quad (\text{A2})$$

According to the OLS method, we can obtain the fitting coefficients α_1 and β_1 for $\text{OLS}(Y|X)$ as

$$\begin{aligned}\alpha_1 &= \frac{C(X_{1i}, X_{2i})}{V(X_{2i})}, \\ \beta_1 &= \bar{X}_{2i} - \alpha_1 \cdot \bar{X}_{1i},\end{aligned}\quad (\text{A3})$$

where

$$\begin{aligned}C(X_{mi}, X_{ni}) &= \sum_{i=1}^N (X_{mi} - \bar{X}_m)(X_{ni} - \bar{X}_n), \\ V(X_{mi}) &= \sum_{i=1}^N (X_{mi} - \bar{X}_m)^2, \\ \bar{X}_m &= \frac{1}{N} \sum_{i=1}^N X_{mi}.\end{aligned}\quad (\text{A4})$$

Similarly, one can obtain the coefficients α_2 and β_2 for $\text{OLS}(X|Y)$, and the coefficients α_{RMA} and β_{RMA} for OLS-RMA can be defined as (for details, see Isobe et al. 1990)

$$\begin{aligned}\alpha_{\text{RMA}} &= (\alpha_1 \alpha_2)^{1/2}, \\ \beta_{\text{RMA}} &= \bar{Y}_2 - \alpha_{\text{RMA}} \cdot \bar{Y}_1.\end{aligned}\quad (\text{A5})$$

According to Akritas & Bershady (1996), the fitting coefficients for the BCES method can be obtained from the OLS method from

$$\begin{aligned}C(Y_{mi}, Y_{ni}) &= C(X_{mi}, X_{ni}) + \sum_{i=1}^N \epsilon_{mi} \epsilon_{ni}, \\ V(Y_{mi}) &= V(X_{mi}) + \sum_{i=1}^N \epsilon_{mi}^2, \\ \bar{Y}_{mi} &= \bar{X}_{mi}.\end{aligned}\quad (\text{A6})$$

Inserting Equations (A3), (A4), and (A6) into Equations (A5), one can obtain the fitting coefficients $\hat{\alpha}_{\text{RMA}}$, $\hat{\beta}_{\text{RMA}}$ for BCES-RMA fitting.

Now we extend the method for 3D data fitting. Let the variables haveing intrinsic real values be denoted by X_{1i}, X_{2i}, X_{3i} , and the observed data by Y_{1i}, Y_{2i}, Y_{3i} , hence the relation between observed data and the variables is

$$Y_{1i} = X_{1i} \pm \epsilon_{1i}, Y_{2i} = X_{2i} \pm \epsilon_{2i}, \text{ and } Y_{3i} = X_{3i} \pm \epsilon_{3i}. \quad (\text{A7})$$

The linear regression model is formulated as

$$X_{3i} = \alpha' X_{1i} + \beta' X_{2i} + \gamma'. \quad (\text{A8})$$

As in 2D fitting, one can get the coefficients α'_1 , β'_1 , and γ'_1 for $\text{OLS}(Y_3|Y_1, Y_2)$ as follows:

$$\begin{aligned}\beta'_1 &= \frac{C(X_{1i}, X_{3i})C(X_{1i}, X_{2i}) - C(X_{2i}, X_{3i})V(X_{1i})}{C^2(X_{1i}, X_{2i}) - V(X_{1i})V(X_{2i})}, \\ \alpha'_1 &= \frac{C(X_{1i}, X_{3i}) - \beta'_1 \cdot C(X_{1i}, X_{2i})}{V_{1i}}, \\ \gamma'_1 &= \bar{X}_{3i} - \alpha'_1 \cdot \bar{X}_{1i} - \beta'_1 \cdot \bar{X}_{2i}.\end{aligned}\quad (\text{A9})$$

One can also obtain α'_2 , β'_2 , and γ'_2 for $\text{BCES}(Y_1|Y_2, Y_3)$ and α'_3 , β'_3 , and γ'_3 for $\text{BCES}(Y_2|Y_1, Y_3)$, respectively. In principle, the 3D RMA fitting is to search for a plane that can minimize the volume of a rectangular solid whose edges are parallel to the axes Y_1 , Y_2 , and Y_3 . It is not easy, however, to obtain the fitting coefficients analytically. We define 3D OLS-RMA fitting coefficients as

$$\begin{aligned}\alpha'_{\text{RMA}} &= (\alpha'_1 \alpha'_2 \alpha'_3)^{1/3}, \\ \beta'_{\text{RMA}} &= (\beta'_1 \beta'_2 \beta'_3)^{1/3}, \\ \gamma'_{\text{RMA}} &= \bar{Y}_3 - \alpha'_{\text{RMA}} \cdot \bar{Y}_1 - \beta'_{\text{RMA}} \cdot \bar{Y}_2.\end{aligned}\quad (\text{A10})$$

Inserting Equations (A4), (A6), and (A9) into Equations (A10), one can obtain the fitting coefficients $\hat{\alpha}'_{\text{RMA}}$, $\hat{\beta}'_{\text{RMA}}$ and $\hat{\gamma}'_{\text{RMA}}$.

The intrinsic scatter σ^2/dof for 3D fitting is then calculated by (Colafrancesco et al. 2014)

$$\frac{\sigma^2}{\text{dof}} = \frac{\sum_{i=1}^N (r_{3i} - \bar{r}_3)^2 - \sum_{i=1}^N \epsilon_{3i}^2}{N - 3}, \quad (\text{A11})$$

where r_{3i} is the residual

$$r_{3i} = Y_{3i} - \hat{\alpha}'_{\text{RMA}} \cdot Y_{1i} - \hat{\beta}'_{\text{RMA}} \cdot Y_{2i} - \gamma'_{\text{RMA}}, \quad (\text{A12})$$

then χ^2/dof can be written as

$$\frac{\chi^2}{\text{dof}} = \frac{1}{N - 3} \sum_{i=1}^N \frac{r_{3i}^2}{\epsilon_{3i}^2 + \hat{\alpha}'_{\text{RMA}}^2 \epsilon_{1i}^2 + \hat{\beta}'_{\text{RMA}}^2 \epsilon_{2i}^2 + \sigma^2/\text{dof}}. \quad (\text{A13})$$

REFERENCES

- Akritas, M. G., & Bershadsky, M. A. 1996, ApJ, 470, 706
 Arnaud, M., Pratt, G. W., Piffaretti, R., et al. 2010, A&A, 517, A92
 Bacchi, M., Feretti, L., Giovannini, G., & Govoni, F. 2003, A&A, 400, 465
 Basu, K. 2012, MNRAS, 421, L112
 Böhringer, H., Voges, W., Huchra, J. P., et al. 2000, ApJS, 129, 435
 Böhringer, H., Schuecker, P., Guzzo, L., et al. 2004, A&A, 425, 367
 Böhringer, H., Pratt, G. W., Arnaud, M., et al. 2010, A&A, 514, A32
 Bonafede, A., Giovannini, G., Feretti, L., Govoni, F., & Murgia, M. 2009a, A&A, 494, 429
 Bonafede, A., Intema, H. T., Brüggen, M., et al. 2014a, ApJ, 785, 1
 Bonafede, A., Feretti, L., Giovannini, G., et al. 2009b, A&A, 503, 707
 Bonafede, A., Brüggen, M., van Weeren, R., et al. 2012, MNRAS, 426, 40
 Bonafede, A., Intema, H. T., Brüggen, M., et al. 2014b, MNRAS, 444, L44
 Brentjens, M. A. 2008, A&A, 489, 69
 Brown, S., Duesterhoeft, J., & Rudnick, L. 2011, ApJ, 727, L25
 Brunetti, G., Cassano, R., Dolag, K., & Setti, G. 2009, A&A, 507, 661
 Brunetti, G., & Jones, T. W. 2014, International Journal of Modern Physics D, 23, 30007
 Brunetti, G., Venturi, T., Dallacasa, D., et al. 2007, ApJ, 670, L5
 Brunetti, G., Giacintucci, S., Cassano, R., et al. 2008, Nature, 455, 944
 Buote, D. A., & Tsai, J. C. 1995, ApJ, 452, 522
 Cassano, R., Ettori, S., Giacintucci, S., et al. 2010, ApJ, 721, L82
 Cassano, R., Gitti, M., & Brunetti, G. 2008, A&A, 486, L31
 Cassano, R., Ettori, S., Brunetti, G., et al. 2013, ApJ, 777, 141
 Clarke, T. E., & Ensslin, T. A. 2006, AJ, 131, 2900
 Colafrancesco, S., Emritte, M. S., Mhlahlo, N., & Marchegiani, P. 2014, A&A, 566, A42
 Cuciti, V., Cassano, R., Brunetti, G., et al. 2015, A&A, 580, A97
 Dallacasa, D., Brunetti, G., Giacintucci, S., et al. 2009, ApJ, 699, 1288
 David, L. P., Forman, W., & Jones, C. 1999, ApJ, 519, 533
 de Gasperin, F., van Weeren, R. J., Brüggen, M., et al. 2014, MNRAS, 444, 3130
 Drabent, A., Hoeft, M., Pizzo, R. F., et al. 2015, A&A, 575, A8
 Ebeling, H., Barrett, E., Donovan, D., et al. 2007, ApJ, 661, L33
 Ebeling, H., Edge, A. C., Allen, S. W., et al. 2000, MNRAS, 318, 333
 Ebeling, H., Edge, A. C., Böhringer, H., et al. 1998, MNRAS, 301, 881
 Ebeling, H., Edge, A. C., Mantz, A., et al. 2010, MNRAS, 407, 83
 Ebeling, H., Mullis, C. R., & Tully, R. B. 2002, ApJ, 580, 774
 Ebeling, H., Voges, W., Böhringer, H., et al. 1996, MNRAS, 281, 799
 Feretti, L., Fusco-Femiano, R., Giovannini, G., & Govoni, F. 2001, A&A, 373, 106
 Feretti, L., Giovannini, G., Govoni, F., & Murgia, M. 2012, A&A Rev., 20, 54
 Feretti, L., Orrù, E., Brunetti, G., et al. 2004, A&A, 423, 111
 Feretti, L., Schuecker, P., Böhringer, H., Govoni, F., & Giovannini, G. 2005, A&A, 444, 157
 Giacintucci, S., Dallacasa, D., Venturi, T., et al. 2011a, A&A, 534, A57
 Giacintucci, S., Kale, R., Wik, D. R., Venturi, T., & Markevitch, M. 2013, ApJ, 766, 18
 Giacintucci, S., Markevitch, M., Brunetti, G., Cassano, R., & Venturi, T. 2011b, A&A, 525, L10
 Giacintucci, S., Markevitch, M., Brunetti, G., et al. 2014a, ApJ, 795, 73
 Giacintucci, S., Markevitch, M., Venturi, T., et al. 2014b, ApJ, 781, 9
 Giacintucci, S., Venturi, T., Brunetti, G., et al. 2009a, A&A, 505, 45
 Giacintucci, S., Venturi, T., Cassano, R., Dallacasa, D., & Brunetti, G. 2009b, ApJ, 704, L54
 Giacintucci, S., Venturi, T., Brunetti, G., et al. 2005, A&A, 440, 867
 Giacintucci, S., Venturi, T., Macario, G., et al. 2008, A&A, 486, 347
 Giovannini, G., Bonafede, A., Feretti, L., et al. 2009, A&A, 507, 1257
 Giovannini, G., & Feretti, L. 2000, New Astro., 5, 335
 Giovannini, G., Feretti, L., & Stanghellini, C. 1991, A&A, 252, 528
 Giovannini, G., Feretti, L., Venturi, T., Kim, K.-T., & Kronberg, P. P. 1993, ApJ, 406, 399
 Govoni, F., Feretti, L., Giovannini, G., et al. 2001, A&A, 376, 803
 Govoni, F., Murgia, M., Feretti, L., et al. 2005, A&A, 430, L5
 Hoeft, M., & Brüggen, M. 2007, MNRAS, 375, 77
 Isobe, T., Feigelson, E. D., Akritas, M. G., & Babu, G. J. 1990, ApJ, 364, 104
 Kale, R., Dwarakanath, K. S., Bagchi, J., & Paul, S. 2012, MNRAS, 426, 1204
 Kale, R., Venturi, T., Giacintucci, S., et al. 2013, A&A, 557, A99
 —. 2015, A&A, 579, A92
 Kang, H., & Ryu, D. 2013, ApJ, 764, 95
 Kim, K.-T., Kronberg, P. P., Dewdney, P. E., & Landecker, T. L. 1990, ApJ, 355, 29
 Kocevski, D. D., Ebeling, H., Mullis, C. R., & Tully, R. B. 2007, ApJ, 662, 224
 Liang, H., Hunstead, R. W., Birkinshaw, M., & Andreani, P. 2000, ApJ, 544, 686
 Lindner, R. R., Baker, A. J., Hughes, J. P., et al. 2014, ApJ, 786, 49
 Macario, G., Markevitch, M., Giacintucci, S., et al. 2011, ApJ, 728, 82
 Macario, G., Venturi, T., Brunetti, G., et al. 2010, A&A, 517, A43
 Mantz, A., Allen, S. W., Ebeling, H., Rapetti, D., & Drlica-Wagner, A. 2010, MNRAS, 406, 1773
 Mazzatorta, P., & Giacintucci, S. 2008, ApJ, 675, L9
 Menanteau, F., Hughes, J. P., Sifón, C., et al. 2012, ApJ, 748, 7
 Motl, P. M., Hallman, E. J., Burns, J. O., & Norman, M. L. 2005, ApJ, 623, L63
 Murgia, M., Govoni, F., Feretti, L., & Giovannini, G. 2010, A&A, 509, A86
 Pandey-Pommier, M., Richard, J., Combes, F., et al. 2013, A&A, 557, A117
 Piffaretti, R., Arnaud, M., Pratt, G. W., Pointecouteau, E., & Melin, J.-B. 2011, A&A, 534, A109
 Pizzo, R. F., & de Bruyn, A. G. 2009, A&A, 507, 639
 Planck Collaboration, Ade, P. A. R., Aghanim, N., et al. 2014a, A&A, 571, A20
 —. 2014b, A&A, 571, A29
 —. 2015, ArXiv e-prints
 Poole, G. B., Fardal, M. A., Babul, A., et al. 2006, MNRAS, 373, 881
 Popesso, P., Böhringer, H., Brinkmann, J., Voges, W., & York, D. G. 2004, A&A, 423, 449
 Press, W. H., Teukolsky, S. A., Vetterling, W. T., & Flannery, B. P. 1992, Numerical recipes in FORTRAN. The art of scientific computing
 Reiprich, T. H., & Böhringer, H. 2002, ApJ, 567, 716
 Riseley, C. J., Scaife, A. M. M., Oozeer, N., Magnus, L., & Wise, M. W. 2015, MNRAS, 447, 1895
 Santos, J. S., Rosati, P., Tozzi, P., et al. 2008, A&A, 483, 35
 Shimwell, T. W., Brown, S., Feain, I. J., et al. 2014, MNRAS, 440, 2901
 Shimwell, T. W., Markevitch, M., Brown, S., et al. 2015, MNRAS, 449, 1486
 Storm, E., Jeltema, T. E., & Rudnick, L. 2015, MNRAS, 448, 2495
 Trasatti, M., Akamatsu, H., Lovisari, L., et al. 2015, A&A, 575, A45
 Vacca, V., Feretti, L., Giovannini, G., et al. 2014, A&A, 561, A52
 Vacca, V., Govoni, F., Murgia, M., et al. 2011, A&A, 535, A82
 van Weeren, R. J., Bonafede, A., Ebeling, H., et al. 2012a, MNRAS, 425, L36
 van Weeren, R. J., Brüggen, M., Röttgering, H. J. A., & Hoeft, M. 2011a, MNRAS, 418, 230

- van Weeren, R. J., Brüggen, M., Röttgering, H. J. A., et al. 2011b, *A&A*, 533, A35
- van Weeren, R. J., Hoeft, M., Röttgering, H. J. A., et al. 2011c, *A&A*, 528, A38
- van Weeren, R. J., Röttgering, H. J. A., Brüggen, M., & Hoeft, M. 2010, *Science*, 330, 347
- van Weeren, R. J., Röttgering, H. J. A., Intema, H. T., et al. 2012b, *A&A*, 546, A124
- van Weeren, R. J., Röttgering, H. J. A., Bagchi, J., et al. 2009, *A&A*, 506, 1083
- van Weeren, R. J., Intema, H. T., Lal, D. V., et al. 2014, *ApJ*, 786, L17
- Venturi, T., Bardelli, S., Dallacasa, D., et al. 2003, *A&A*, 402, 913
- Venturi, T., Giacintucci, S., Brunetti, G., et al. 2007, *A&A*, 463, 937
- Venturi, T., Giacintucci, S., Dallacasa, D., et al. 2008, *A&A*, 484, 327
- . 2013, *A&A*, 551, A24
- Venturi, T., Giovannini, G., & Feretti, L. 1990, *AJ*, 99, 1381
- Vikhlinin, A., Burenin, R. A., Ebeling, H., et al. 2009, *ApJ*, 692, 1033
- Voges, W., Aschenbach, B., Boller, T., et al. 1999, *A&A*, 349, 389
- Weißmann, A., Böhringer, H., Šuhada, R., & Ameglio, S. 2013, *A&A*, 549, A19
- Wen, Z. L., & Han, J. L. 2013, *MNRAS*, 436, 275
- . 2015, *ApJ*, 807, 178
- Wen, Z. L., Han, J. L., & Liu, F. S. 2012, *ApJS*, 199, 34
- Wik, D. R., Sarazin, C. L., Ricker, P. M., & Randall, S. W. 2008, *ApJ*, 680, 17
- Zhao, H.-H., Jia, S.-M., Chen, Y., et al. 2013, *ApJ*, 778, 124
- Zhao, H.-H., Li, C.-K., Chen, Y., Jia, S.-M., & Song, L.-M. 2015, *ApJ*, 799, 47
- ZuHone, J. A., Markevitch, M., Brunetti, G., & Giacintucci, S. 2013, *ApJ*, 762, 78